ADAPTIVE OPTICS FOR IMPROVED MODE-COUPLING EFFICIENCIES

BY

SCOTT M. JOBLING

B.S., University of Massachusetts at Lowell, 2006

THESIS

Submitted in partial fulfillment of the requirements
for the degree of Master of Science in Electrical and Computer Engineering
in the Graduate College of the
University of Illinois at Urbana-Champaign, 2008

Urbana, Illinois

Adviser:

Professor Paul G. Kwiat

ABSTRACT

Low insertion loss is a critical requirement for some newly emerging applications, such as optical quantum computing. We have demonstrated improved free-space to single-mode fiber coupling via wavefront correction using an adaptive-optic (AO) mirror. By introducing AO correction paired with a three-step optimization algorithm, we have obtained $97.3 \pm 0.3\%$ of the Fresnel-reflection-limited mode-coupling efficiency. Our optimization scheme utilizes wavefront sensing for close-loop correction of wavefront aberrations, followed by evolutionary and convex maximization of coupled power. We have further shown a 9-nm RMS wavefront flatness through close-loop correction, limited only by the AO mechanical tolerances, as well as similar flatness utilizing only coupled-power optimization.

To Mother and Father, and to others who have provided guidance for so long.

ACKNOWLEDGMENTS

I owe a great deal of thanks to my adviser, Paul Kwiat, for all the time he has dedicated to my work over the past two years and for his thorough and constructive review of this thesis. I am very grateful for the opportunity to be involved in a research group led by someone who is as objective, understanding, and tirelessly curious as he is. I am also indebted to each of my group members for setting such a high standard for achievement, and for providing friendships that have contributed to a great working experience. In particular, I want to thank Ria and Kevin for their review and feedback while preparing this document. Also, thanks to Scott Carney, whose consistent availability and frank discussions have shed light on many of the technical details supporting this work. Finally, thanks to my family and friends, those who know me best, for their enduring encouragement and understanding throughout this process.

TABLE OF CONTENTS

LIST OF FIGURES

LIST OF ABBREVIATIONS

AO	Adaptive optics
BS	Beamsplitter
DM	Deformable mirror
HG	Hermite-Gauss modes
LP	Linear-polarization modes
MO	Microscope objective
PBS	Polarizing beamsplitter
PSI	Phase-shift interferometry
QWP	Quarter-wave plate
SHS	Shack-Hartmann sensor
SMF	Single-mode fiber
SR	Strehl ratio
SVD	Singular-value decomposition
TEM	Transverse electromagnetic
VSI	Vertical-shift interferometry

LIST OF SYMBOLS

η	Coupling efficiency
λ	Wavelength
$\phi(\mathbf{r})$	Generalized phase (complex-amplitude representation)
$\boldsymbol{\phi}_k$	Measured wavefront
σ	Intensity-weighted RMS wavefront mismatch for two modes
$\zeta(z)$	Guoy phase of a Gaussian beam
$a(\mathbf{r})$	Generalized amplitude of $U(\mathbf{r})$
$\mathbf{A}$	Mirror influence function
$\mathbf{A}^+$	Pseudo-inverse of the mirror influence function
$H_n()$	Hermite polynomial of order n
$J_l()$	Bessel function of the first kind of order l
$K_l()$	Modified Bessel function of the second kind of order l
k	Wavevector
$\mathrm{R(z)}$	Radius of curvature of a Gaussian beam
$\mathbf{S}$	Singular values (SVD)
$\mathbf{U}$	Wavefront basis vectors (SVD)
$U(\mathbf{r})$	Generalized scalar field (complex-amplitude representation)
$\mathbf{v_k}$	Set of mirror command voltages
$\mathbf{V}$	Command-voltage basis vectors (SVD)
$w(z)$	Beamwaist of a Gaussian beam
$\mathbf{Z_{l,m}}$	Zernike polynomial of order l and index m

CHAPTER 1

INTRODUCTION

Low insertion loss has long been a desired characteristic of most fiber- and integrated-optic components. Such losses are unacceptable for some newly emerging applications. For example, practical implementation of optical quantum computing will require integrated optics with fully optimized components and low-loss interconnects. When dealing with waveguides such as single-mode optical fibers and integrated optics, interconnection losses can become rather significant and result primarily from mode-alignment and mode-mismatch issues. It is therefore necessary to ensure that all losses are accounted for and minimized. For fault-tolerant operation of quantum computing, cascaded error correction is necessary to reach a given accuracy [1, 2]. As the reliability of transmission throughout an optical system is reduced, the necessary resources for these cascaded operations increase rapidly.

While alignment losses can be straightforwardly addressed, mode-mismatch losses generally require more difficult correction techniques, such as ball-lens coupling [3], waveguide end tapering [4], or adaptive-optic (AO) mode-correction [5, 6]. Black-box solutions such as lens coupling typically suffer losses of 20-50%, while solutions like tapering boast losses as low as 1.5-4% with the caveat of requiring modified components and much higher cost. Here we present an AO approach for minimizing the coupling losses between two single-mode optics, e.g., a free-space Gaussian beam and a single-mode fiber (SMF), through both alignment and wavefront corrections. We achieved the latter through evolutionary-algorithm

optimization of a deformable-membrane mirror. Accounting for Fresnel losses in the optics, we were able to reduce coupling losses in an aligned system from 5.6% to 2.7%.

This work serves as a partial demonstration of the limits of correction possible through the utilization of adaptive optics for mode coupling. However, it is certainly not practical to implement an AO system at every interconnect. Rather, it is necessary to know the bounds which are limiting system performance, so that we might establish practical and realistic expectations. In light of this need, the system presented here has been designed to operate with wavefront-limited performance. Total mode correction (including the transverse intensity profile) is a significantly more complex problem, as will be discussed in Chapter 3, and represents the next phase of our experiment.

It is necessary to make use of a number of tools and techniques in order to accomplish the task of implementing AO wavefront correction. The first set of techniques to be discussed here involve wavefront sensing, or the measurement of optical fields which are not directly observable. Without such information there is no way of definitively showing that a coupling system is wavefront limited, and that any AO correction is indeed working. There are a number of methods and applications of wavefront sensing within AO, and we will provide an overview in Chapter 2. Equally important to the recognition of a need for correction is an understanding of the problem of coupling light between propagating modes. Chapter 3 provides an overview of the optics and optical issues relevant to mode coupling and AO optimization.

In order to develop a successful AO system, we must assess the correction needs and available components. Chapter 4 provides an overview of the numerous types of optics, as well as techniques, available for adaptive control. It is essential for single-mode coupling that the components and design be chosen carefully for

successful implementation. Although AO correction provides the capability to compensate for many practical shortcomings, it is useless without proper placement and control. We discuss the experimental layout and testing in Chapter 5, which serves as an overall summary of our demonstration. There are a number of potential modifications and extensions to this work, which are reviewed in Chapter 6, e.g., systems that are limited by intensity rather than wavefront mismatch.

Since the first introduction of AO correction in astronomy, the technology has been evolving to meet new challenges and specifications. Only recently, however, have components become available which are scaled to a practical size for bulk-optics interfacing at visible wavelengths, rather than in the infrared or longer regimes appropriate for astronomy and satellite communication. This work shows the potential for utilizing this new generation of AO components to improve systems that are otherwise operating at the practical limit. An AO approach represents a generic solution to such problems, and can provide valuable and needed insight into a system's ultimate practical potential.

CHAPTER 2

OPTICAL WAVEFRONT SENSING

2.1   Introduction

It is possible, through proper experimental setup (e.g., alignment, optimized coatings, etc.), to restrict losses in a coupling system to only those caused by wavefront mismatch. Wavefront mismatch is a measure of how well a field's wavefront, as defined by a chosen plane of constant phase, matches that of another field or mode. Unfortunately, there are no antennae appropriately scaled for optical wavelengths, and thus no direct method for measuring an optical field or wavefront.

As mentioned earlier, it is partly the goal of this work to demonstrate the proof-of-principle operation of an adaptive-optic mirror's correction of wavefront mismatch. This begs the question, how does one evaluate the correction of a system limited by an immeasurable field? The answer lies in the heart of optical wavefront sensing, in which an optical field can be *inferred* from how it behaves. There are a number of different methods for obtaining this information, and it is important to consider each in proper context as none is a direct measurement.

2.2 Wavefronts

2.2.1 Optics by the book

In order to properly introduce the concepts involved in wavefront sensing, it is necessary to first discuss the theory upon which wavefront sensing is founded. Like so many discussions of electromagnetics, ours begins with Maxwell's equations. Our formulation follows that of Born and Wolf in [7], which presents a detailed analysis tailored for optics, though this analysis is presented in many texts in various forms. For electromagnetic fields, we have the following relationships (in Gaussian units):

$$\nabla \times \mathbf{H} - \frac{1}{c}\frac{d}{dt}\mathbf{D} = \frac{4\pi}{c}\mathbf{j}, \tag{2.1}$$

$$\nabla \times \mathbf{E} - \frac{1}{c}\frac{d}{dt}\mathbf{B} = 0, \tag{2.2}$$

$$\nabla \cdot \mathbf{D} = 4\pi\rho, \tag{2.3}$$

$$\nabla \cdot \mathbf{B} = 0. \tag{2.4}$$

Equations (2.1)-(2.4) comprise Maxwell's equations in differential form, where $\mathbf{E}$, $\mathbf{H}$, $\mathbf{D}$, and $\mathbf{B}$ are the electric and magnetic fields and flux-densities, respectively. Also included in this representation are the electric charge and current densities, which act as sources. This set of equations explicitly defines the behavior of, and balancing between, all electromagnetic fields. However, deriving analytical solutions for any given situation from this point can be difficult to potentially impossible. In the interest of solving practical problems, it is often necessary to account for material properties and specific wavelengths, from which another set of equations, the constitutive relations, arise. To first order, we have:

$$\mathbf{j} \;=\; \hat{\sigma}\mathbf{E}, \tag{2.5}$$

$$\mathbf{D} \;=\; \hat{\epsilon}\mathbf{E}, \tag{2.6}$$

$$\mathbf{B} \;=\; \hat{\mu}\mathbf{H}, \tag{2.7}$$

where we have introduced $\hat{\sigma}$, $\hat{\epsilon}$, and $\hat{\mu}$, respectively the conductivity, electric permittivity (or dielectric constant), and magnetic permeability. In a general sense, each parameter is defined based on an applicable medium and frequency, and need not be scalar. A more complete analysis would include higher order terms as well, to account for high-intensity fields. Fortunately, in low-intensity free-space optics we can greatly simplify our analysis without sacrificing accuracy through a few assumptions. For our purposes we can safely assume that we are dealing with source-free, isotropic, nonconducting media, for which $\mathbf{j} = \rho = \hat{\sigma} = 0$, and both $\hat{\epsilon}$ and $\hat{\mu}$ become direction-independent scalars ϵ and μ. It should be emphasized that although such assumptions are valid for a wide array of problems (e.g., geometrical optics), this is not a thorough treatment of optical theory. From this basis, however, we can proceed to develop a suitable representation of an optical field for our work.

2.2.2 The complex-amplitude representation

If we reconsider Maxwell's equations in light of the assumptions made in the previous section, it can be seen that the electric and magnetic vector components possess conveniently symmetric forms. It now becomes possible to derive the Helmholtz wave equation through a series of clever manipulations. By appropriate substitutions and application of time-derivative and curl operators, Eqs. (2.1)-(2.7) can be written:

$$\nabla^2 \mathbf{H} - \frac{\epsilon\mu}{c^2}\frac{d^2}{dt^2}\mathbf{H} + (\nabla \ln\epsilon) \times (\nabla \times \mathbf{H}) + \nabla(\mathbf{H} \cdot \nabla \ln\mu) = 0, \qquad (2.8)$$

$$\nabla^2 \mathbf{E} - \frac{\epsilon\mu}{c^2}\frac{d^2}{dt^2}\mathbf{E} + (\nabla \ln\mu) \times (\nabla \times \mathbf{E}) + \nabla(\mathbf{E} \cdot \nabla \ln\epsilon) = 0. \qquad (2.9)$$

Equations (2.8) and (2.9) can be further simplified by recalling that an isotropic medium implies scalar permittivities and permeabilities, i.e., $\nabla ln\epsilon = \nabla ln\mu = 0$, which yields the wave equation as promised:

$$\nabla^2 \mathbf{H} - \frac{\epsilon\mu}{c^2}\frac{d^2}{dt^2}\mathbf{H} = 0, \qquad (2.10)$$

$$\nabla^2 \mathbf{E} - \frac{\epsilon\mu}{c^2}\frac{d^2}{dt^2}\mathbf{E} = 0. \qquad (2.11)$$

From this point on we dispense with discussing in particular either the electric or magnetic fields, as Eqs. (2.10) and (2.11) are quite symmetric for both fields and a generalized vector field would suffice. Assuming a Cartesian coordinate system, however, we can also dispense with any further vector analysis, as the Laplacian operator acts upon each dimension independently. We can thus proceed to consider only a generalized scalar field, V, which satisfies the wave equation as in Eq. (2.12), and can be extrapolated to any component of the electric or magnetic field.

$$\nabla^2 V - \frac{\epsilon\mu}{c^2}\frac{d^2}{dt^2}V = 0. \qquad (2.12)$$

We can now develop a convenient form for a solution to Eq. (2.12) which is relevant to our work. If we consider real-valued monochromatic fields, one solution which can be obtained is

$$V(\mathbf{r}, t) = a(\mathbf{r})cos[\omega t - \phi(\mathbf{r})] \qquad (2.13)$$

for a real scalar amplitude, $a(\mathbf{r}) > 0$, and real phase, $\phi(\mathbf{r})$. This can now be

rewritten taking advantage of complex exponentials for a monochromatic harmonic field.

$$V(\mathbf{r}, t) = Re[U(\mathbf{r})e^{-i\omega t}], \tag{2.14}$$

$$U(\mathbf{r}) = a(\mathbf{r})e^{i\phi(\mathbf{r})}. \tag{2.15}$$

Similar to the vector treatment of the field, it is no longer necessary to consider the explicit time dependence of the field. It is possible to remove this from our analysis by reminding ourselves that we are considering only monochromatic and real fields, and only linear materials. The time dependence can be included as a final step as shown in Eq. (2.14). We are then left with the so-called complex-amplitude representation of the generalized field in Eq. (2.15) which fully describes a field of known wavelength.

It is worthwhile to briefly discuss the intuitive structure of the complex-amplitude representation given in Eq. (2.15). In this form we have conveniently separated the amplitude and phase of a field. Though the actual measurement of such a field proves more difficult in the optical regime, as will be discussed, this structure allows both amplitude and phase components to be determined simultaneously from the real and imaginary parts of a field. If we then consider fixed values for the phase, $\phi(\mathbf{r}) = const.$, there are surfaces periodic in phase which provide an identical contribution to the field, i.e., $\phi(\mathbf{r}) = \phi_0 = \phi_0 + 2\pi = \ldots = \phi_0 + 2\pi n$. An example of this is illustrated in Fig. 2.1 for an arbitrary phase distribution. These surfaces are commonly referred to as wavefronts, or isophase planes, and are analogous to the peaks and troughs of physical waves.
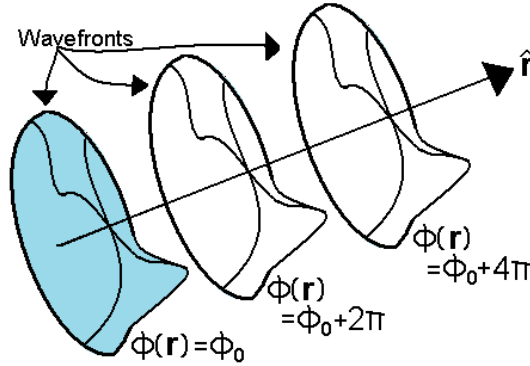
Figure 2.1: Illustration of wavefronts for an arbitrary phase distribution.

2.3   Detecting Wavefronts

If a tree falls in the woods, and no one is around, does it make a sound?

– Anonymous

Yes, indirect observation can establish that a falling tree is accompanied by quite a racket. With light, only the intensity of a field is typically observable, leaving us blind to the subtleties hidden within the phase; this can impact problems such as mode-coupling. However, there are ways of "chopping down" the field and forcing its inherent properties to reveal wavefront information. Two methods are discussed here — namely, interferometric and Shack-Hartmann — which have both developed hand-in-hand with the maturing of AO systems.

2.3.1   Interferometers

Perhaps the most direct methods for measuring wavefront information are those which involve interferometry. Interference phenomena appear in a broad class of systems, and many other interesting behaviors such as diffraction and imaging can be broken down in terms of collective interference from many sources [7]. We are concerned with a straightforward view of interference, in which the magnitude of two quasi-monochromatic interacting fields differs from the sum of the magnitudes

of the independent fields [8]. For example, consider the intensity resultant from the sum of two fields [9], and the complex-amplitude representation of the fields:

$$I(\mathbf{r}) = |U(\mathbf{r})|^2 = |U_1(\mathbf{r}) + U_2(\mathbf{r})|^2, \tag{2.16}$$

$$U_n(\mathbf{r}) = \sqrt{I_n(\mathbf{r})}e^{i\phi_n(\mathbf{r})}. \tag{2.17}$$

Substituting Eq. (2.17) into Eq. (2.16) and simplifying (note the explicit positional dependence has been dropped for brevity) gives

$$
\begin{aligned}
I &= U_1^*U_1 + U_2^*U_2 + U_1^*U_2 + U_2^*U_1 \\
&= I_1 + I_2 + 2\sqrt{(I_1 I_2)}cos(\phi_2 - \phi_1). \tag{2.18}
\end{aligned}
$$

Equation (2.18) implies that the measurable intensity now has a phase dependence due to interference. Also, we must know both the independent intensities a priori in order to calculate the phase relationship at any given point.

This direct approach has proven vital for a number of applications, e.g., to characterize detailed surfaces rather than wavefronts. Phase-shift interferometry (PSI – see Appendix A) and Twyman-Green interferometers are typical examples of such an application [8]. With these techniques, light is partially transmitted through a beamsplitter, reflected off or through an object, and recombined with the diverted portion of the light which has propagated an identical distance. The change in the intensity pattern generated is due entirely to the phase accumulated in the transmitted path; i.e., it is due to the object.

Here, we are interested in wavefronts, not objects or surfaces. The above-mentioned techniques effectively remove wavefront information for well-matched path lengths by the nature of the relative phase relationship. Other applications based on this approach will yield wavefront information, however, by making two

simple changes: removing any wavefront-altering objects, and requiring different paths such that the beams are slightly displaced relative to one another. This is the basis for shearing interferometry, and represents a measurement of the local phase-gradient along the direction of displacement. For equivalent but displaced fields, Eq. (2.18) becomes Eq. (2.19).

$$
\begin{aligned}
I(\mathbf{r}) &= U^*(\mathbf{r_1})U(\mathbf{r_1}) + U^*(\mathbf{r})U(\mathbf{r}) + U^*(\mathbf{r_1})U(\mathbf{r}) + U^*(\mathbf{r})U(\mathbf{r_1}) \\
&= I(\mathbf{r_1}) + I(\mathbf{r}) + 2\sqrt{(I(\mathbf{r_1})I(\mathbf{r})}cos(\phi(\mathbf{r}) - \phi(\mathbf{r_1})).
\end{aligned}
\tag{2.19}
$$

Again, we have that for known intensity distributions we can back out the phase change over a known displacement: the interference patterns relate to the phase-gradient, which can then be used to reconstruct the wavefront via integration. In theory, two orthogonal scans are necessary and sufficient for a complete reconstruction, although more scans [10] or further modifications such as the use of diffraction gratings [11] can be used to create a more robust reconstruction.

2.3.2 Shack-Hartmann sensors

Another way of obtaining wavefront information is the use of a Shack-Hartmann sensor, which is a device designed to analyze the behavior of small sections of a wavefront within the regime of geometrical optics. To build up this analysis, we assume the paraxial approximation, in which all propagating light is sufficiently parallel to the optical axis. As pointed out by many [7, 8, 12], this is equivalent to assuming that all relevant incidence angles with the optical axis satisfy the small angle approximation $(sin(\theta) \approx \theta)$. Under this assumption, all light passing through a lens focuses within the same plane, though the position on the plane is determined directly by the angle of incidence (Fig. 2.2).

In order to extend this concept to the domain of wavefront sensing, first con-
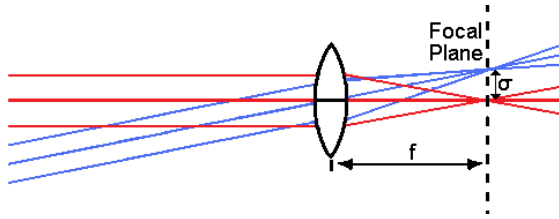
Figure 2.2: Focusing of light under the paraxial approximation.

sider the position of the focal point as a measurement of a flat wavefront with a constant tilt perpendicular to the rays drawn (and very poor sampling!). Although any fluctuations in the wavefront will undoubtedly distort the focal point, we must consider the tilt as an average of the wavefront over the aperture (or pupil) of the lens. By assuming that there are negligibly small aberrations other than tilt, we have effectively created a tilt-detecting wavefront sensor with a tilt perpendicular to the angle of incidence: $\theta = tan^{-1}(\sigma/f) \approx (\sigma/f)$.

Finally, consider the curved wavefront shown in Fig. 2.3, where we can increase the resolution and create a basic Shack-Hartmann sensor (SHS) by introducing additional lenses. Each lens samples a small portion of the wavefront to obtain a *local* tilt, equivalent to the local phase-gradient. From this point, reconstructing the wavefront is a matter of integration and appropriate interpolation. It is important to note that there are important limits associated with an SHS, as well as a number of details which have been discussed here in principle rather than rigorously. A discussion of these details is provided at the end of the chapter.

2.4   Using Wavefronts for Feedback

Given the ability to determine propagating wavefronts in a system, the question of how to best use this information arises. For real-time AO systems, wavefront sensing is often implemented as part of active feedback for control over an adaptive element. In systems which require peak performance, or Strehl Ratios (SRs)
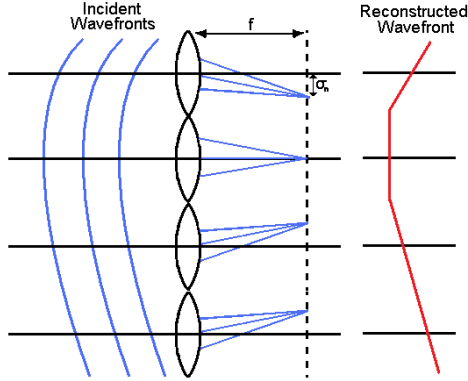
Figure 2.3: In-principle operation of a Shack-Hartmann sensor.

greater than $\sim$0.95, wavefront characterization is a useful tool for testing performance before and after correction. A hybrid of the two methods is also possible, with the wavefront sensor providing active feedback as an initial step, followed by some metric-based optimization scheme.

The distinction between each implementation of wavefront feedback ultimately depends on the required accuracy and speed. Wavefront analysis can simultaneously provide information about the action of each degree of freedom related to an adaptive element as quickly as the information can be processed. However, the information is bound by tolerances associated with the sensor, such as physical alignment, sampling, and reconstruction quality. Blind-optimization schemes, e.g., those which optimize a performance metric and need no knowledge of a system, can correct an AO system to within the true performance limit of the optics, and sometimes with a more simplistic design. Furthermore, such schemes are capable of correcting situations in which an optimal target is not known. Without a priori knowledge or wavefront feedback, however, blind optimization schemes are dramatically slower and require a proper control algorithm designed to guarantee global convergence.

There are many AO systems that make use of one or both of these approaches for wavefront feedback. Fernández et al. [13] and Li et al. [14] demonstrate two

examples in which wavefront analysis is used as part of the correction scheme with very good performance (average reported SRs of 0.94 and 0.92, respectively). In experiments involving single-mode optical coupling, such as those performed by Gonté [5] and Plett [6], wavefront sensing is used to characterize the initial and settled systems, and optimization algorithms are used for correction. Coupling experiments are very susceptible to small alignment errors and are difficult to compare to pure wavefront correction. Since wavefront measurements are performed in the image plane of an "object" on the scale of 5 μm, the required large magnifications – fast lenses – increase the potential for error.

Our own work serves as an example of the differences between the two mentioned strategies. As we discuss in greater detail in Chapter 5, we have utilized active feedback for wavefront correction to obtain a calculated SR (from the RMS wavefront) of 0.98; however, the measured SR (from the single-mode coupling) was 0.94. Through blind optimization, we are able to obtain a calculated SR of 0.96 and measured SR of greater than 0.97; however, much more run-time is required. Despite careful optical alignment, there are still appreciable differences between the two techniques, especially considering the order of magnitude difference in the convergence times. Ultimately, we mostly employ blind optimization as our primary concern is efficiency, not speed.

2.5   Capabilities and Limitations

As there are many different wavefront sensing systems available, it is not appropriate to discuss specific device characteristics at this point. However, there are theoretical assumptions which apply to most wavefront sensors which we can now discuss. Although we have presented a reasonable and accurate approach, it is important to consider the practical limitations imposed by such assumptions. In

some cases a robust design can compensate for pushing a system beyond these limits. We are concerned with Shack-Hartmann sensors, though interferometric methods are not without limitations, of course. Briefly, many difficulties with interferometric measurements arise when considering the sensitivity of interference patterns to optical vibrations and alignment, as well as measurement sensitivities with CCD cameras. In order for interferometric sensors to reach the accuracy of Shack-Hartmann sensors, typically $\lambda/100$ or better, more complex implementations than described previously are necessary. Such improvements also involve additional measurements and mechanical systems [10, 11], thus reducing the capability to operate the device in real-time.

For Shack-Hartmann sensors, we consider the assumption that we are operating within the limits of geometrical optics, e.g., wavelengths which are much smaller than the scale of the optical system ($\lambda \to 0$), which is very well satisfied for our work. Small perturbations which arise in practical systems can be treated within the realm of geometrical optics [7], and will be discussed in Chapter 3. An additional consideration is the impact of these fluctuations on the performance of a wavefront sensor. Shack-Hartmann sensors are typically susceptible to wavefront aberration errors, due to averaging over lens apertures. In this case, high-frequency perturbations are washed out due to sampling, and the focal plane is distorted. Many recent advances in SHS have been in the development of "microlenses" to alleviate the sampling concerns. To account for focal plane distortion, high-density CCD arrays are used to measure the distribution of the focal point, or the *centroid*. There are numerous algorithms dedicated to analyzing centroids [15], though a simple first-moment calculation is sufficiently accurate for most scenarios. Regardless of the centroiding technique, we must take care to assure that the measured wavefronts are adequately sampled for the averaging to be representative.

We consider the paraxial approximation next, which was necessary to back out local slopes in an SHS for wavefront reconstruction. Two issues relating to the sensor design and field behavior arise near the limits of this approximation. As mentioned earlier, high-density lens arrays are used to assure sufficient sampling in modern sensors. As the incident local slope increases (larger tilt), the focal point distribution begins to overlap the CCD sensors for adjacent lenses, wreaking havoc on centroid algorithms. To avoid such a problem it is common to install irises which reduce stray light, as well as to develop alignment-failure tests within SHS control software. Another consideration when nearing the limit of paraxial propagation is the introduction of aberrations due to the lenses; however, this falls within the distortions correctable via centroiding. As a note, the paraxial restriction can be greatly relaxed with more complex implementations and processing schemes [16, 17], though this is unnecessary for our work.

The remaining approximations applicable to Shack-Hartmann sensors involve the device construction and wavefront reconstruction. A typical SHS consists of an array of lenses and a CCD camera which are carefully calibrated for any mechanical errors. This calibration is often performed using a well-defined wavefront [15], such as that out of a single-mode fiber, and the residual error is often provided as part of a device's specifications. The resulting reconstructed wavefronts, on the other hand, vary depending on software and preference. In the simplest form, reconstructed wavefronts are rough interpretations, as seen in Fig. 2.3. Such a linear reconstruction is not physical, as propagating fields have continuous wavefronts. Alternative reconstruction methods such as Zernike polynomial fitting, however, offer valuable physical insight into optical systems, at the cost of accuracy. In general the reconstruction process is only as accurate as the experimental raw data, and any alternative reconstruction methods should be used cautiously.

CHAPTER 3

MODE COUPLING

3.1   Introduction

The concept of modes in optics evolved from attempts to describe propagating fields, be they in free space or well-defined structures, although the term "mode" is more closely related to eigenmodes and the broad subject of linear systems. An eigenmode is any input with fundamental properties which remain unchanged after passing through a given system, while modes are superpositions of eigenmodes. In a broad sense, the music through a quality audio system and the image through a camera lens are collections of modes. Similarly, there are modes for many optical systems which have very practical applications. For example, satellite systems utilize free-space modes to communicate, and fiber-optic communications rely on modes to carry information unchanged across continents and under oceans.

The modes involved in various systems can have a profound impact on overall efficiency when such systems are combined. Simply because an input is an eigenmode for one system, it is not necessarily an eigenmode for another. The ability to couple light between different systems can be fully described in terms of how well the eigenmodes for one overlap that of another. Here we present an overview of optical modes and their relationship to coupling efficiencies.

3.2 Free Space, Fibers, and Waveguides

As stated above, there are a number of different systems which occur often in optics and photonics, each of which is accompanied by a unique set of eigenmodes. For our current and future work, we are concerned with the modes for free space and waveguides (of which fibers are a relevant example). We work with single-mode systems, or those in which only one eigenmode is present. For example, the structure and properties of waveguides can be designed to only allow a single propagating eigenmode, always the lowest-order or "fundamental" mode. Beyond the paraxial approximation, as described in Chapter 2, there are no such restrictions in free space, and we must take care to prevent more than one eigenmode from becoming excited.

3.2.1 Free-space modes

Consider the paraxial Helmholtz equation, as written in Eq. (2.12), which describes the propagation of light in free space. We can rewrite this relationship for a scalar field by accounting for the implicit time dependence in Eq. (2.14):

$$(\nabla^2 + \epsilon\mu k^2)U = 0, \tag{3.1}$$

where $k = \omega/c$ is the wavenumber for the field, and we can assume $\epsilon = \mu = 1$ in free space. We are concerned with fields that not only propagate, e.g., those of the form in Eq. (2.15), but that reproduce themselves throughout propagation. One recognizable example is that of the Gaussian beam, so named because its intensity distribution is that of a Gaussian function (see Fig. 3.1). The derivation of the Gaussian form can be found in many places [8, 9, 18], and is little more than creatively expanding on a paraboloidal solution to Eq. (3.1). From such an

18
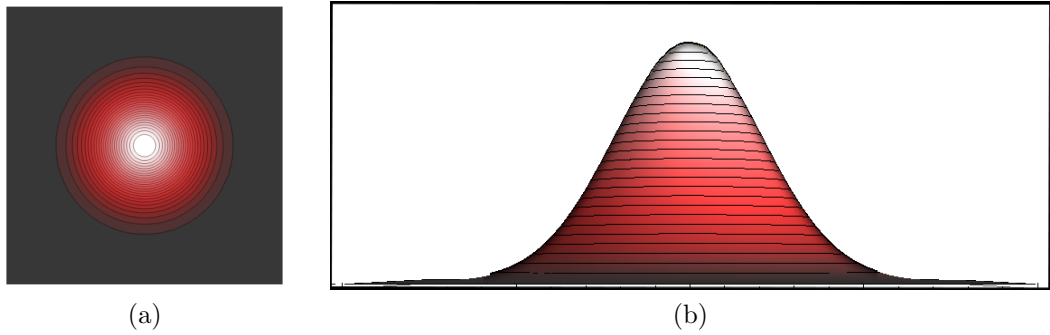
Figure 3.1: Contour plots of the intensity of a Gaussian beam.

approach, the spatial dependence of the field takes the form

$$U(\mathbf{r}) = a_0 \left[\frac{w(0)}{w(z)} \right] e^{-\frac{(x^2+y^2)}{w^2(z)}} e^{-ikz - ik\frac{(x^2+y^2)}{2R(z)} + i\zeta(z)}. \tag{3.2}$$

We have expressed the field in terms of common beam parameters $w(z)$, $R(z)$, and $\zeta(z)$, or the beamwaist, radius of curvature, and Guoy phase, respectively. The beamwaist describes the radius at which the field amplitude drops to $1/e$ of the peak value, with $w(0)$ usually defined as the minimum beamwaist. The curvature describes the spherical shape of the wavefront, and the Guoy phase represents the phase delay of the field compared to a plane wave. These few properties are sufficient to fully describe the field throughout propagation, and thus Eq. (3.2) is a mode of free space.

The Gaussian beam is not the only solution to the paraxial Helmholtz equation; it is possible to describe any field distribution in terms of modes. Much as any spatial coordinate can be completely described in a chosen orthogonal basis, such as (x, y, z) or (ρ, ϕ, θ), we can describe any paraxial field in terms of a number of complete sets, or bases. That is, any paraxial field can be expressed as a sum of eigenmodes, and a set of eigenmodes which can describe any field is considered to be complete. It is necessary to use infinitely many modes to construct such a basis, unfortunately, though a number of solutions are readily available.

Hermite-Gauss (HG) modes, for example, form one possible complete set [9]:

$$U_{l,m}(\mathbf{r}) = a_{l,m} \left[\frac{w(0)}{w(z)}\right] G_l \left[\frac{\sqrt{2}x}{w(z)}\right] G_m \left[\frac{\sqrt{2}y}{w(z)}\right] e^{-ikz - ik\frac{(x^2+y^2)}{2R(z)} + i(l+m+1)\zeta(z)}, \quad (3.3)$$

$$G_n(u) = H_n(u)e^{-\frac{u^2}{2}},$$

where $H_n(u)$ are the Hermite polynomials, and we have assumed propagation along the $\hat{z}$ direction. For the fundamental mode, $l = m = 0$, we again have the Gaussian beam described in Eq. (3.2), though the field quickly becomes complicated as the order increases. The intensity distributions of some lower-order Hermite-Gauss modes can be seen in Fig. 3.2. It is essential to avoid higher-order modes for our work, as there is nothing inherent to free space to prevent such modes from being propagating solutions to the wave equation.
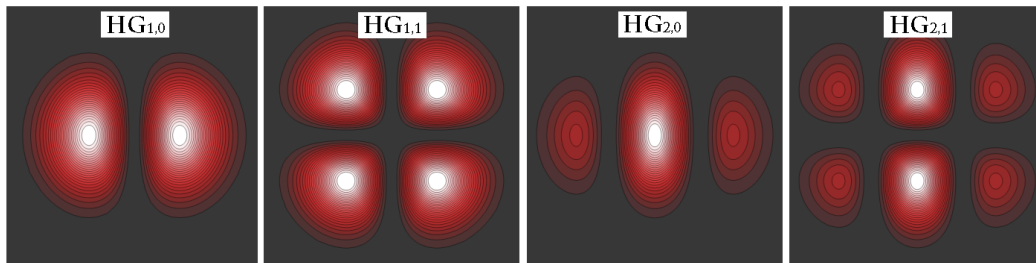
Figure 3.2: Example contour plots of the intensities for HG modes.

3.2.2   Guided modes

We return to the paraxial Helmholtz equation to describe guided modes, only now we assume a coordinate system appropriate to the guiding structure. Here we provide an overview – more rigorous treatments can be found in Chuang [19] and Saleh and Teich [9]. The derivation of guided modes follows that of free-space modes, expanding the description to include material and symmetry changes. For example, fiber modes are most easily derived in a cylindrical coordinate system.

We can simplify the problem of solving the Helmholtz equation by including the guiding direction and any inherent symmetry in the general form of the field:

$$U(\mathbf{r}) = a(r)e^{-il\phi}e^{-i\beta z}, \tag{3.4}$$

where l is an integer and we have assumed a cylindrically periodic field propagating in the $\hat{z}$ direction. By introducing two additional parameters, k_T and γ, we can find an expression for the amplitude of a guided field after substitution into Eq. (3.1):

$$a(r) \propto \begin{cases} J_l(k_T r) & , \quad r < a \\ K_l(\gamma r) & , \quad r > a \end{cases}, \tag{3.5}$$

$$k_T^2 = n_1^2 k_0^2 - \beta^2, \tag{3.6}$$

$$\gamma^2 = \beta^2 - n_2^2 k_0^2, \tag{3.7}$$

where J_l is the Bessel functions of the first kind and K_l is the modified Bessel function of the second kind, both of order l. As discussed in [9], the field is guided so long as both k_T and γ are positive. Although the form of the field provided by Eqs. (3.4) and (3.5) provides a picture of fiber modes in a general sense, there is still a great deal of complexity involved in solving for all components of the field when considering boundary conditions. A more common and practical approach involves the weakly guiding fiber approximation, in which the index change between the core and cladding is assumed to be very small ($\Delta n \ll 1$), as is the case for modern fiber optics. In this regime, any longitudinal field components become insignificant, and the supported fields can be considered TEM waves with two orthogonal polarizations. Since we have only transverse fields, the boundary conditions need only be applied to the magnitude of the field, which reduces the problem to solving a single characteristic equation with a number
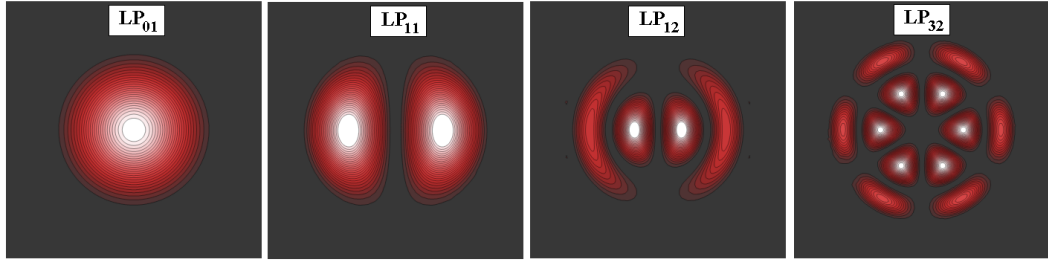
Figure 3.3: Example contour plots of the intensities for LP modes.

of transcendental solutions. The solutions to this approach yield the so-called linear-polarization (LP) modes [20], although there is no particular restriction to linear polarizations. The LP modes have a structure defined by both the azimuthal parameter l mentioned earlier, and the order of the transcendental solution, denoted m. The intensity distributions of LP and HG modes are very similar for low orders (compare Figs. 3.2 and 3.3), though the similarities vanish quickly as the order increases.

The general waveguide modes can always be determined by following the process outlined for fibers. Unfortunately, elegant solutions such as LP modes are an exception to the typical waveguide problem. Still, there are known solutions to most common waveguide structures, such as the rectangular waveguide outlined by Chuang in [19], even if the form is more complicated. The simplest solutions reflect the guiding symmetry: circular waveguides result in Bessel modes, while rectangular waveguides have two-dimensional sinusoidal modes, both with guiding in the core and exponential decay in the cladding. Further analysis becomes a matter of applying material properties to a particular geometry.

3.3   Modal Analysis of Coupling

Once we have obtained expressions for the modes of various optical systems, it is important to understand the limitations of coupling between different systems.

Consider the modal expansion of a normalized field:

$$U(\mathbf{r}) = \sum_m c_m u_m(\mathbf{r}), \text{ where} \tag{3.8}$$

$$\int d\mathbf{r} \; |u_m(\mathbf{r})|^2 = 1, \text{ and} \tag{3.9}$$

$$\sum_m c_m = 1. \tag{3.10}$$

As mentioned earlier, we cannot describe a mode, u_m, by any collection of other (orthogonal) modes in the same basis. However, it is possible to describe a mode in one basis in terms of the modes in another basis. If we consider a guiding medium in terms of a possibly incomplete set of modes, the coupling efficiency can be thought of as the overlap between the input and guiding modes. For example, a collection of HG modes passing through a spatial filter will only couple the modes which are supported by the spatial filter, e.g., the fundamental mode. However, any paraxial system will couple with maximum efficiency to free space, which supports all propagating modes as discussed earlier.

We can now write the coupling efficiency in terms of a given set of basis functions, $\{b_n(\mathbf{r})\}$; the modal expansion of the field is then

$$\eta(\{c_m u_m\}, \{b_n\}) = \left| \sum_n \sum_m c_m \int d\mathbf{r} \; u_m(\mathbf{r}) b_n^*(\mathbf{r}) \right|^2. \tag{3.11}$$

When the basis functions are equivalent to the modes of the starting medium, the integral in Eq. (3.11) becomes equivalent to Eq. (3.9), and $\eta = 1$. Also, if the set $\{b_n\}$ is complete, the summation over n is guaranteed to converge to unity. Lastly, we have defined the efficiency based on measurable power, which requires that we work with the square of the field.

The modal approach is a powerful tool for understanding the requirements for

coupling into a certain medium, as well as for manipulating the field algebraically. However, modal analysis can easily become overly complicated if care is not taken to choose the proper set of basis functions; a field which requires an infinite expansion in the HG basis might be described by a single mode in another, for example.

3.4   Aberrations and Apodizations

It is of particular interest to our work to understand the impact that small perturbations of the field can have on coupling, especially to evaluate AO correction in the high-efficiency limit. Although it is possible to experimentally limit the intensity apodizations, the wavefront aberrations are inherent to the optics in use. Since these perturbations to the field may require a very large number of eigenmodes to be accurately described, it is not convenient to consider the general case of coupling efficiency in terms of modal decompositions. For two complex-amplitude scalar fields (Eq. (2.15)), we can redefine the coupling efficiency from Eq. (3.11) for the case when $m = n = 1$:

$$U(\mathbf{r}) = a(\mathbf{r})\Phi(\mathbf{r}), \tag{3.12}$$

$$\eta(U_1(\mathbf{r}), U_2(\mathbf{r})) = \frac{\left|\int d\mathbf{r} \ U_1(\mathbf{r})U_2^*(\mathbf{r})\right|^2}{\int d\mathbf{r} \ |U_1(\mathbf{r})|^2 \ \int d\mathbf{r} \ |U_2(\mathbf{r})|^2}. \tag{3.13}$$

Note that the modes do not need to be normalized in this definition. Substituting Eq. (3.12) into Eq. (3.13)and multiplying by a convenient form of one, we can

rewrite the efficiency in terms of the Strehl ratio (SR):

$$\eta(U_1(\mathbf{r}), U_2(\mathbf{r})) = \frac{\left|\int d\mathbf{r}\ a_1\Phi_1\ a_2\Phi_2^*\right|^2}{\int d\mathbf{r}\ |a_1\Phi_1|^2\ \int d\mathbf{r}\ |a_2\Phi_2|^2}, \tag{3.14}$$

$$= \frac{\left|\int d\mathbf{r}\ a_1\Phi_1\ a_2\Phi_2^*\right|^2}{\int d\mathbf{r}\ |a_1|^2\ \int d\mathbf{r}\ |a_2|^2} \cdot \frac{\left|\int d\mathbf{r}\ a_1\ a_2\right|^2}{\left|\int d\mathbf{r}\ a_1\ a_2\right|^2}, \tag{3.15}$$

$$= \frac{\left|\int d\mathbf{r}\ a_1\ a_2\right|^2}{\int d\mathbf{r}\ |a_1|^2\ \int d\mathbf{r}\ |a_2|^2} \cdot \frac{\left|\int d\mathbf{r}\ a_1\Phi_1\ a_2\Phi_2^*\right|^2}{\left|\int d\mathbf{r}\ a_1\ a_2\right|^2}, \tag{3.16}$$

$$= \eta(a_1, a_2) \cdot SR(U_1 \cdot U_2). \tag{3.17}$$

The Strehl ratio is a measure of the peak intensity of aberrated beams when perfectly focused. The SR can be written many ways; here we adapt a form similar to that from Born and Wolf [7]:

$$SR(U(\mathbf{r})) = \frac{\left|\int d\mathbf{r}\ U(\mathbf{r})\right|^2}{\int d\mathbf{r}\ |U(\mathbf{r})|^2}. \tag{3.18}$$

3.4.1 Wavefront perturbations

We have made no assumptions about aberrations at this point, and we can now consider two limiting cases. First, when the two modes possess perfect wavefront matching, i.e., $SR(U_1 \cdot U_2) = 1$, we have a coupling efficiency purely dependent on the magnitude overlap of the two modes. Second, and of more interest to our work, if we have perfect intensity overlap, i.e., $\eta(a_1, a_2) = 1$, the coupling efficiency takes on an interesting dependence on both magnitude and phase:

$$\eta(U_1(\mathbf{r}), U_2(\mathbf{r})) = \frac{\left|\int d\mathbf{r}\ a^2(\mathbf{r})\Phi_1(\mathbf{r})\ \Phi_2^*(\mathbf{r})\right|^2}{\left|\int d\mathbf{r}\ a^2(\mathbf{r})\right|^2}. \tag{3.19}$$

It is possible to further simplify this relationship by making the assumption that the coupling efficiency is sufficiently high ($\eta > 0.8$). We follow an example

similar to that laid out in Born and Wolf for aberrated plane waves, which was further elaborated by Mahajan in [21]. We begin by rewriting Eq. (3.19) to include the explicit phase dependence:

$$\eta(U_1(\mathbf{r}), U_2(\mathbf{r})) = \frac{\left| \int d\mathbf{r} \, a^2(\mathbf{r}) e^{\frac{i2\pi\phi_1(\mathbf{r})}{\lambda}} e^{\frac{-i2\pi\phi_2(\mathbf{r})}{\lambda}} \right|^2}{\left| \int d\mathbf{r} \, a^2(\mathbf{r}) \right|^2}, \tag{3.20}$$

$$= \frac{\left| \int d\mathbf{r} \, a^2(\mathbf{r}) e^{\frac{i2\pi(\phi_1(\mathbf{r}) - \phi_2(\mathbf{r}))}{\lambda}} \right|^2}{\left| \int d\mathbf{r} \, a^2(\mathbf{r}) \right|^2} = \frac{\left| \int d\mathbf{r} \, a^2(\mathbf{r}) e^{\frac{i2\pi(\Delta\phi(\mathbf{r}))}{\lambda}} \right|^2}{\left| \int d\mathbf{r} \, a^2(\mathbf{r}) \right|^2}.$$

We can rewrite the denominator of Eq. (3.20) as a normalization term, A^2, and rewrite the exponential via a truncated Taylor series:

$$\approx \left| \int d\mathbf{r} \, \frac{a^2(\mathbf{r})}{A} \left\{ 1 + i\frac{2\pi}{\lambda}\Delta\phi(\mathbf{r}) + \frac{1}{2}\left(i\frac{2\pi}{\lambda}\Delta\phi(\mathbf{r}) \right)^2 \right\} \right|^2, \tag{3.21}$$

$$\approx \left| \frac{\int d\mathbf{r} \, a^2(\mathbf{r})}{A} + i\frac{2\pi}{\lambda} \int d\mathbf{r} \, \frac{a^2(\mathbf{r})}{A}\Delta\phi(\mathbf{r}) \right.$$

$$\left. -\frac{1}{2}\left(\frac{2\pi}{\lambda} \right)^2 \int d\mathbf{r} \, \frac{a^2(\mathbf{r})}{A}(\Delta\phi(\mathbf{r}))^2 \right|^2. \tag{3.22}$$

If we first consider $a(\mathbf{r})$ to be constant, a close inspection of Eq. (3.22) reveals that each integral yields the spatial average of the integrand. If we include the normalized intensity, this instead yields an intensity-weighted spatial average of the integrand [21]. Rewriting Eq. (3.22) in terms of the average values gives

$$\eta(U_1(\mathbf{r}), U_2(\mathbf{r})) = \left| 1 + i\frac{2\pi}{A\lambda}\overline{a^2(\mathbf{r})\Delta\phi} - \frac{1}{2A}\left(\frac{2\pi}{\lambda} \right)^2 \overline{a^2(\mathbf{r})(\Delta\phi)^2} \right|^2, \tag{3.23}$$

$$= 1 - \left(\frac{2\pi}{\lambda} \right)^2 \left(\overline{Aa^2(\mathbf{r})(\Delta\phi)^2} - \left(\overline{Aa^2(\mathbf{r})\Delta\phi} \right)^2 \right), \tag{3.24}$$

$$= 1 - \left(\frac{2\pi}{\lambda} \right)^2 \sigma^2, \tag{3.25}$$
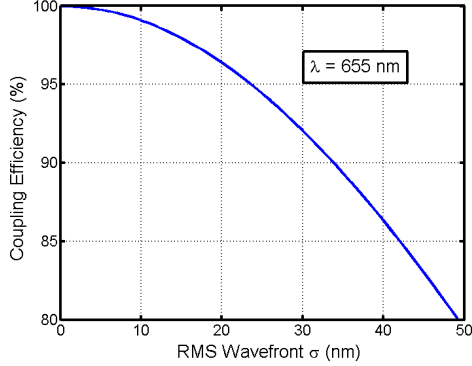
Figure 3.4: Coupling-efficiency dependence on RMS mismatch for uniform intensity.

where we have used $\overline{\{\ \}}$ to indicate the average of a function over the integrating area, and σ to indicate the intensity-weighted root-mean-square (RMS) wavefront mismatch over the aperture defined by $a(\mathbf{r})$. Note that we have dropped any terms higher than second order and applied a standard definition of the RMS value of a function to arrive at Eq. (3.25). Noting the similarity of Eq. (3.25) to the Taylor expansion of an exponential, we can make one final approximation within the high-efficiency limit, after which the coupling efficiency takes the following form (Fig. 3.4):

$$\eta(U_1(\mathbf{r}), U_2(\mathbf{r})) \approx e^{-(\frac{2\pi\sigma}{\lambda})^2}. \tag{3.26}$$

Equation (3.26) allows us to quickly interpret an aberrated wavefront's impact on the coupling efficiency, without the need for performing any intensive calculations. Interestingly, it has been shown that although nearly equivalent for $SR \geq 0.8$, the approximation of the Strehl ratio in Eq. (3.26) is more accurate than Eq. (3.25) for estimating the Strehl ratio for $SR \geq 0.3$ [21] (though only accurate to within 10% for $SR \leq 0.8$).

27

3.4.2 Zernike aberration modes

Lastly, we discuss a modal formulation for wavefronts, in which it is possible to express any wavefront through one of an infinite number of different complete bases [7]. It is of particular interest to highlight the Zernike polynomials, which are the widely accepted standard for describing aberrations over a circular aperture. The popularity of the Zernike basis follows from its usefulness in describing common optical aberrations, as well as its being fundamentally invariant to rotations and having many known applications from early work developed by Zernike, Nijoboer, Wolf, and others.

The lower-order Zernike polynomials, i.e., focus, astigmatism, coma, and spherical aberration, approximately represent the primary, or Seidel aberrations (see Fig. 3.5), although a strict definition would also include intensity as well as the distortion aberration. It is convenient to consider the primary aberrations as part of a complete basis, although each can be derived through a power-series expansion of a wavefront [7]. For our purposes, we work with the Zernike aberrations, and references to the primary aberrations refer to the corresponding Zernike modes.

Also, the primary aberrations are common to typical optical systems; tilt and focus are parameters for ideal optical components such as lenses and mirrors, for example. Spherical aberration results from the deviation between the ideal parabolic and realistic spherical shapes in lenses and mirrors. Astigmatism and coma aberrations are common to physical systems with slight alignment errors, and can often be corrected with symmetric balancing. Since the Zernike basis is complete, it is possible to describe an arbitrary wavefront to any desired accuracy while simultaneously revealing important properties about an optical system. Overall, we have a number of tools at our disposal which provide insight not only

into the problem of coupling, but also into the potential for AO correction.
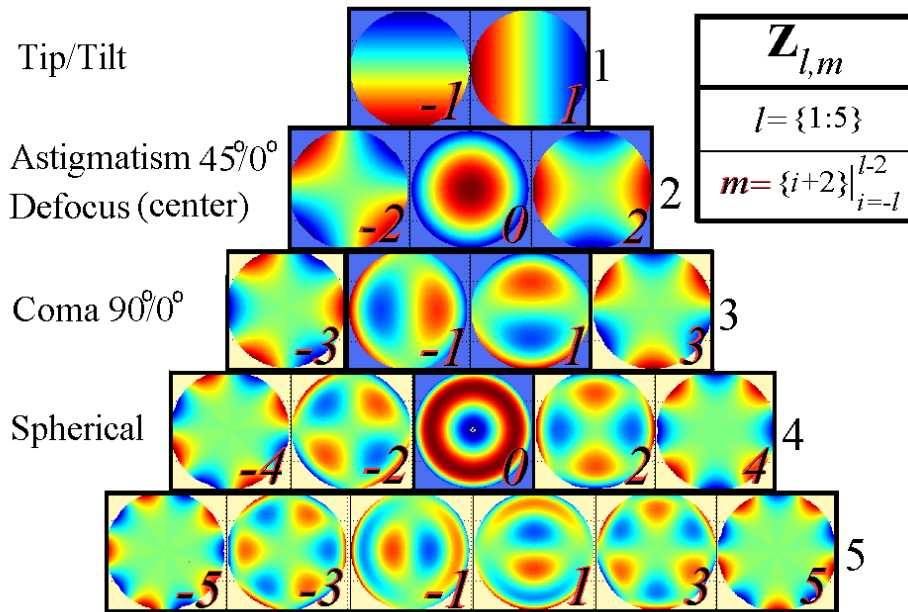
Figure 3.5: Example Zernike aberration plots up to fifth order. The common/primary aberrations are named and highlighted in blue.

CHAPTER 4

ADAPTIVE OPTICS

4.1   Introduction

As shown in Chapter 3, we are fundamentally limited by how well we can match the intensities and wavefronts of two sets of supported modes. Given a system which requires maximum performance, we must evaluate just how well we can compensate for any aberrations and apodizations. If we can modify the wavefront with high efficiency, we can straightforwardly correct any aberrations. Apodizations, however, requires a more complicated process. Consider the magnification of a mode with a planar wavefront, shown in Fig. 4.1, as an example of an apodization correction. The imaging system should perform two functions: modify the wavefront to reshape the mode through propagation, and adjust the wavefront to correct the mode after propagation. Within the diffraction limit, we suspect that any apodization can be corrected with high efficiency by introducing an appropriate number of wavefront adjustments, though our example required only two. We thus have a potential method for total mode correction by introducing only wavefront perturbations.

Since *our* goal of performing mode correction is to increase the coupling efficiency between two modes, it is essential that the correction process itself be highly efficient. There are a number of different kinds of optics which can efficiently alter the wavefront of a mode: lenses, mirrors, phase plates, etc. However, unlike adaptive optics, none of these offers a dynamic solution for the problem
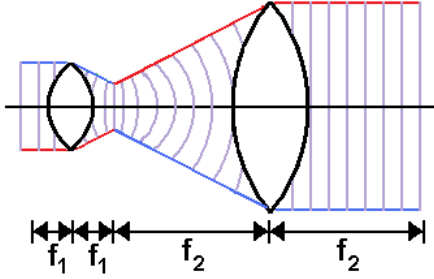
Figure 4.1: 4-f type imaging system with magnification.

of mode correction. There are a number of different adaptive elements available
such as acousto-optic modulators (AOMs), liquid-crystal spatial-light modulators
(SLMs), reflective microelectromechanical systems (MEMS) segmented mirrors,
as well as deformable-membrane mirrors (DMs).

We can eliminate AOMs and SLMs from consideration due to the high-
efficiency requirements of our system. Acousto-optic devices rely on very small
index changes, which makes for excellent diffraction properties under Bragg con-
ditions [9], but poor local phase control. SLMs, which are arrays of liquid-crystal
cells with voltage-dependent phase delays, have yet to become highly efficient
— commercial SLMs are typically below 90% efficient [22, 23], despite innovative
modifications to reduce fill-factor and polarization effects [24]. Alternatively, both
segmented and membrane mirrors rely only on a reflective surface, making them
ideal candidates for mode correction.

4.2   Adaptive Mirrors

Adaptive-optic mirrors possess the unique simplicity of reflective surfaces for the
implementation of wavefront correction. By utilizing appropriate reflection coat-
ings, the upper limit on adaptive-mirror performance is set only by design and
manufacturing quality. The two fundamental classes of adaptive mirrors are seg-
mented mirrors, which use arrays of independently controlled mirrors, and mem-

brane mirrors, which utilize a deformable and continuous reflective surface. Modern segmented mirrors are almost exclusively built up from MEMS technology, while membrane mirrors are often hybrids of MEMS structures and larger optical components.

4.2.1   Segmented mirrors

MEMS technology encompasses a broad class of devices and techniques which implement micron-scale mechanical structures via micromachining. Manufacturing techniques are based on current semiconductor technologies, allowing for a wide range of processes from deposition and etching to lithography and substrate bonding [25]. Segmented mirrors have a number of advantages over deformable-membrane mirrors. Manufacturing costs are typically much lower for MEMS technology [26], with the entire process supported by standard fabrication techniques. The utilization of state-of-the-art facilities also allows for intricate designs and high actuator densities, as well as surface fill-factors approaching 100%. The design of the mirrors further allows for independent control of each segment, which reduces control-scheme complexities by virtually eliminating cross-talk across the mirror surface.

We have evaluated the performance of a segmented MEMS mirror for possible incorporation in a mode-correction system. The device, pictured in Fig. 4.2, was a 61-element polysilicon mirror with piston/tip/tilt actuation on each element, and was provided by Sandia National Labs (see [26]). Unfortunately, our testing indicated that such segmented mirrors are not yet a sufficiently mature technology for high-efficiency coupling, for a number of reasons. As discussed by Dagel et al. [26], the manufacturing process creates individual elements with slight residual curvatures (60-nm bow per element), which by itself eliminates
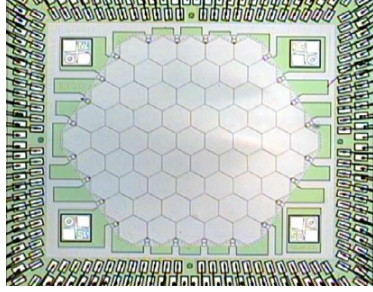
Figure 4.2: 61-element segmented MEMS mirror.

this particular device from consideration. We could either impose a permanent focus, matching the element curvature, to compensate, or allow a minimum of at least 30-nm RMS aberrations (see Fig. 3.4), neither of which is an acceptable option for our purposes. Additionally, each individual element is driven by cantilever-piezo actuators, which leads to significant nonlinearity and hysteresis, as well as a performance change when reflective coatings are added, due to additional element curvature and more sluggish responses due to the sensitivity of the cantilever design. Although there are other commercial segmented mirrors available, such as that by IrisAO, performance evaluations of these have revealed similar shortcomings with residual RMS error [27].

The high densities and low cost of segmented mirrors make the technology a very attractive prospect for many applications such as beam steering and beam splitting in higher-speed, lower-SR systems. However, for future applications in high-efficiency coupling, segmented mirrors remain only a possibility. Immediate drawbacks such as residual RMS error and actuator nonlinearities need to be overcome in order to realize high enough efficiencies for coupling systems.

4.2.2 Deformable-membrane mirrors

In contrast to segmented mirrors, there are numerous manufacturing techniques and technologies currently in use for membrane mirrors. It is possible to sim-

ply cover a piezo-based structure with a continuous surface, as is done for some mirrors by OKO Technologies [27]. Piezoelectric mirrors are further separated by actuator densities and layouts, with hexagonal and rectangular structures commonly available. Similar to piezo structures, bio-inspired (or "biomorph") mirrors by AOptix utilize electroresistive layers to form a deformable surface driven by arrays of electrodes [28]. Membrane mirrors are based on an array of electrodes pushing and pulling a membrane via its electrostatic response, e.g., from AgilOptics and Boston Micromachines. Lastly, Imagine Optic has implemented a unique magnetic-coil design to provide the necessary actuation via magnetic induction. Two arrays of magnets, one made of permanent magnets fixed to the membrane, the other made of electromagnets fixed to driving circuitry, are used to drive the mirror.

(a) Mirror unit.   (b) Actuator layout.
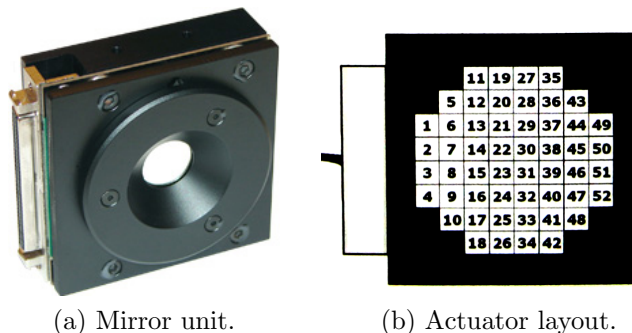
Figure 4.3: The Mirao52D membrane deformable mirror.

For our work, we have made use of the Mirao52D by Imagine Optic (Fig. 4.3), which has 52 actuators positioned in a grid over a circular area. The Mirao52D is the best available AO mirror with respect to specified RMS errors, as confirmed by Devaney et al. [27], who measured the performance of several AO mirrors. Compared to other available mirrors with RMS errors on the order of 50 to 100 nm, the Mirao52D can obtain better than 10-nm RMS flatness and 20-nm RMS error for the generation of up to fifth-order Zernikes [29] (see Chapter 3). Recalling
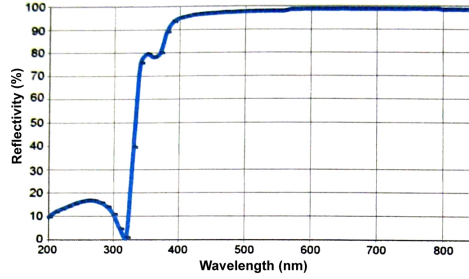
Figure 4.4: Reflectivity spectrum for the Mirao52D mirror.

Eq. (3.26), these errors result in a theoretical upper limit of $\eta \approx 96.5\%$ for arbitrary wavefront correction at visible wavelength. We are further restricted by the intrinsic reflectivity of the protective silver membrane itself (see Fig. 4.4), although the reflectivity is better than 98% over the range $560 - 850$ nm.

4.3   Mirror Control Algorithms

Beyond simply having a deformable mirror, we also require a method for *controlling* the mirror in our adaptive system. As mentioned earlier, we can perform any arbitrary mode correction through appropriate wavefront modifications. We must therefore understand how well we can perform a single wavefront correction in order to predict how well we can scale such a process, as discussed in Chapter 1. We have developed a three-step process effective for wavefront correction using wavefront-feedback and metric-based optimization techniques.

4.3.1   Close-loop algorithm

Close-loop operation is intended to be a first correction of the aberrations in an optical system. Although there are many techniques for "closing the loop," as discussed in Chapter 2, we use a Shack-Hartmann sensor (SHS) for providing the necessary feedback to our system. For optimal performance, it is necessary

to image any aberration-inducing optics onto the surface of the DM, as well as to image the DM onto the SHS. In this way, any aberrations present can be corrected by adjusting the mirror, and any deformations of the mirror can be measured by the SHS. If care is not taken in this process, aberrations of field will induce apodizations during propagation, which in turn will interfere with both the SHS measurements and the coupling efficiency. For example, aberrations due to a grating-like surface would form a diffraction pattern during propagation, which cannot be corrected in a single-step wavefront adjustment. However, imaging such a grating onto the DM surface enables the mirror to cancel any diffraction effects, assuming the mirror can exactly match the conjugate shape of the grating.

Our close-loop process is implemented via the CASAO software suite, provided by Imagine Optic [29], though the general process is a straightforward application of linear algebra. First, we choose a set of command voltages, represented by an n-dimensional column vector, $\mathbf{v_k}$, where each element of $\mathbf{v_k}$ relates to one of the $n = 52$ degrees of freedom for the Mirao52D. We can also measure the wavefront resultant from the set of command voltages, represented by m-dimensional column vector, $\boldsymbol{\phi}_k$, where each element of $\boldsymbol{\phi}_k$ relates to a component of the output wavefront, i.e., a coordinate on the wavefront sensor or a modal amplitude in a chosen basis. In general, n, the number of accessible degrees of freedom of the mirror, will be different than the number of parameters characterizing the wavefront. We can express this relationship, illustrated in Fig. 4.5, in matrix form:

$$\left(\boldsymbol{\phi}_k\right)_{m\times 1} = \left(\mathbf{A}\right)_{m\times n} \left(\mathbf{v_k}\right)_{n\times 1}, \tag{4.1}$$

where $\mathbf{A}$, also referred to as the influence function, is a linear operator which represents the action of the command voltages on the wavefront, and is initially unknown.
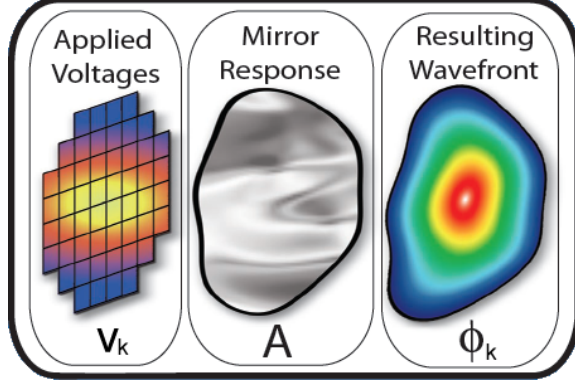
Figure 4.5: Visual of AO response to command voltages.

It is possible to determine **A** by "mapping" each command voltage element onto a measured wavefront. For example, in order to characterize our mirror, we need to apply 52 sets of command voltages and measure 52 wavefronts. We can express this process as

$$
\begin{pmatrix} \phi_1 & \cdots & \phi_n \end{pmatrix}_{m \times n} = \begin{pmatrix} \mathbf{A} \end{pmatrix}_{m \times n} \begin{pmatrix} \mathbf{v_1} & \cdots & \mathbf{v_n} \end{pmatrix}_{n \times n}, \tag{4.2}
$$

where the collection of command voltages should test each mirror degree of freedom independently, i.e., the collection should form an orthonormal basis. The wavefronts are typically sampled at a much higher resolution than the input ($m \gg n$), so it can be useful to first project the wavefront onto a finite basis ($m' \lesssim n$) to reduce the calculation intensity. For example, our Shack-Hartmann wavefront sensor has a default resolution of 1280 elements which we could project onto a finite basis of 52 Zernikes without losing significant accuracy. To calculate this projection, we must determine the operator, **B**, which best maps a set of Zernike basis-function coefficients, $\mathbf{Z_{k'}}$, onto a given wavefront, $\phi_{k'}$. We begin with the relationship between the basis functions and wavefronts:

$$
\begin{pmatrix} \phi_{k'} \end{pmatrix}_{m \times 1} = \begin{pmatrix} \mathbf{B} \end{pmatrix}_{m \times m'} \begin{pmatrix} \mathbf{Z_{k'}} \end{pmatrix}_{m' \times 1}, \tag{4.3}
$$

where the primed indices are included to emphasize the limitations of the finite basis, which may not produce a perfect wavefront fit. Note the similarity between Eqs. (4.1) and (4.3). Since we have closed-form expressions for each of the basis functions, we can calculate the mapping of the basis functions onto the wavefronts, and subsequently determine the operator **B** before ever making any measurements:

$$\left(\mathbf{B} \right)_{m \times m'} = \left(\phi_{1'} \quad \cdots \quad \phi_{m'} \right)_{m \times m'} \left(\mathbf{Z}_{1'} \quad \cdots \quad \mathbf{Z}_{\mathbf{m'}} \right)^{-1}_{m' \times m'}. \qquad (4.4)$$

It is now possible to calculate the basis coefficients, $\mathbf{Z}_{\mathbf{m'}}$, which best fit a given input wavefront, ϕ_k:

$$\left(\mathbf{Z}_{\mathbf{k'}} \right)_{m' \times 1} = \left(\mathbf{B} \right)^{+}_{m' \times m} \left(\phi_k \right)_{m \times 1}, \qquad (4.5)$$

where we have projected the wavefront, ϕ_k, onto the finite Zernike basis, $\mathbf{Z}$, via the "pseudo-inverse" of the operator **B**, denoted $\mathbf{B}^{+}$. We will discuss the pseudo-inverse in the context of wavefront correction; suffice it to say, this projection results in the best-fit modal amplitudes for the chosen basis. Although this may not seem to reduce calculation time at first glance, we can calculate $\mathbf{B}^{+}$ ahead of time since we know **B** ahead of time, thus reducing the real-time calculation intensity when the finite basis is much smaller than the wavefront resolution.

Since it is our goal to apply some arbitrary wavefront correction, ϕ_0, we need to determine an appropriate set of command voltages, $\mathbf{v_0}$, for the mirror. One could (naively) consider Eq. (4.1) to be sufficient information for determining $\mathbf{v_0}$:

$$\left(\mathbf{v_0} \right)_{n \times 1} = \left(\mathbf{A} \right)^{-1}_{n \times m} \left(\phi_0 \right)_{m \times 1}. \qquad (4.6)$$

Unfortunately, it is easy to construct situations in which Eq. (4.6) fails, e.g., when **A** is not a square matrix, or when the wavefront does not respond to a particular

set of commands, that is, $\phi_k = \{0\}$ in Eq. (4.2). The first situation occurs anytime the wavefront images are over- or undersampled compared to the input ($m \neq n$), which may be due to the choice of basis functions or a voluntary removal of particular modes. For unresponsive modes, the zero-amplitude terms in the influence function would cause $\mathbf{A}^{-1}$ and subsequently $\mathbf{v_0}$ to blow up. Since infinite values are obviously a poor choice for command voltages, a more robust approach to inverting the influence function is to apply a singular-value decomposition (SVD) to calculate its pseudo-inverse, which removes any issues with the problems mentioned. Briefly, SVD is a tool which rewrites a noninvertible rectangular matrix as the product of two unitary matrices and a rectangular matrix with the so-called singular values along the diagonal [30]. This technique was used by Devaney et al. and Dalimier et al. in [27, 28] to perform the mirror testing mentioned earlier, and occurs frequently in AO control [14, 29, 31]. We can calculate $\mathbf{A}$ from Eq. (4.2), and proceed to write the equivalent form via SVD:

$$\mathbf{A}_{m \times n} = \begin{pmatrix} \phi_1 & \cdots & \phi_m \end{pmatrix}_{m \times n} \begin{pmatrix} \mathbf{v_1} & \cdots & \mathbf{v_n} \end{pmatrix}_{n \times n}^{-1} \tag{4.7}$$

$$\Rightarrow \mathbf{USV^T}, \text{ where} \tag{4.8}$$

$$\mathbf{U_{m \times m}} = \text{Eigv.} \left[\mathbf{A}_{m \times n} \mathbf{A}_{n \times m}^T \right], \tag{4.9}$$

$$\mathbf{S_{m \times n}} = \begin{pmatrix} \sigma_1 & & & \\ & \ddots & & \\ & & \sigma_r & \\ & & & 0 \end{pmatrix}, \tag{4.10}$$

$$\mathbf{V_{n \times n}} = \text{Eigv.} \left[\mathbf{A}_{n \times m}^T \mathbf{A}_{m \times n} \right]. \tag{4.11}$$

The columns of $\mathbf{U}$ and $\mathbf{V}$, called the left- and right-singular vectors of $\mathbf{A}$, are the eigenvectors (Eigv.) of the normal operators $\mathbf{AA}^T$ and $\mathbf{A}^T\mathbf{A}$. The singular values, $\boldsymbol{\sigma}_k$, which are along the diagonal of $\mathbf{S}$, are the mutual eigenvalues of the

singular vectors, and can be calculated from any of the following relationships:

$$\left(\mathbf{A} \right)_{m \times n} \left(\mathbf{v_k} \right)_{n \times 1} = \sigma_k \left(\mathbf{u_k} \right)_{m \times 1}, \tag{4.12}$$

$$\left(\mathbf{A} \right)^T_{n \times m} \left(\mathbf{u_k} \right)_{m \times 1} = \sigma_k \left(\mathbf{v_k} \right)_{n \times 1}, \tag{4.13}$$

$$\sigma_k = \| \mathbf{A} \mathbf{v_k} \| = \| \mathbf{A^T} \mathbf{u_k} \|. \tag{4.14}$$

Although it may be less than intuitive from this formulation, an SVD essentially separates what can and cannot be inverted. In other words, we have mapped a collection of command voltages, weighted by the singular values, onto a basis of wavefronts and vice versa. Furthermore, if the weight relating an input and output is zero, we have no control over that output, and should ignore it entirely. If we wish to solve the inverse problem, we only need to invert the nonzero singular values. We can now determine the best set of command voltages to attain a desired wavefront according to what we have calculated the mirror can generate. In contrast to Eq. (4.6), the SVD method provides a reliably invertible solution in the absence of noise (the "pseudo-inverse"):

$$\left(\mathbf{v_{0''}} \right)_{n \times 1} = \left(\mathbf{A} \right)^{+}_{n \times m} \left(\phi_0 \right)_{m \times 1}, \tag{4.15}$$

where the primed index is included on $\mathbf{v_{0''}}$ to remind us of the approximate nature of the inverse problem, similar to the limitation of using a finite Zernike basis to describe a wavefront (Eq. (4.3)). The pseudo-inverse, $\mathbf{A^+}$, is defined as the inverse

of Eq. (4.8) treating $\mathbf{S^{-1}}$ as the transpose of $\mathbf{S}$ inverted over the nonzero diagonal:

$$\left(\mathbf{A}\right)^{+}_{n\times m} = \mathbf{VS^{-1}U^T}, \text{ where} \tag{4.16}$$

$$\mathbf{S^{-1}_{n\times m}} = \begin{pmatrix} \sigma_1^{-1} & & & \\ & \ddots & & \\ & & \sigma_r^{-1} & \\ & & & 0 \end{pmatrix}. \tag{4.17}$$

We are thus left with a set of voltages, $\mathbf{v_{0"}}$, that produce the best possible deformation of the mirror to generate a target wavefront. The best-fit wavefront can be determined by the projection of the desired wavefront mode onto the modes determined in the SVD:

$$\left(\phi_{0"}\right)_{m\times 1} = \left(\mathbf{A}\right)_{m\times n} \left(\mathbf{A}\right)^{+}_{n\times m} \left(\phi_0\right)_{m\times 1}, \tag{4.18}$$

$$= \mathbf{USS^{-1}U^T}\phi_0. \tag{4.19}$$

The power of the SVD is to invert the otherwise uninvertible; using this technique we determine the voltage settings that lead to the smallest deviation (as determined by a least-squares fit) between the desired correction and that actually produced by the deformable mirror. Lastly, by imposing additional criteria in Eq. (4.15), we can create a system which is also robust to noise. Including noise in the formulation introduces small perturbations to the singular matrix, which renders the $\sigma_k \neq 0$ criteria nearly useless. Alternatively, we can impose a threshold ($\sigma_k > \sigma_0$), or filtering techniques such as Tikhonov regularization, which is equivalent to weighting the inverse singular values by a fixed parameter ($\sigma_k^{-1} \rightarrow \frac{\sigma_k}{\sigma_k^2+\lambda}$) [32, 33].

The close-loop optimization technique is a very fast process, and can provide a

great deal of insight into the aberrations present. Practically speaking, however, we need to divert the propagating light in order to measure the system aberrations, which introduces two problems: we must have a different optical path to the wavefront sensor, and we must remove the wavefront sensor and its associated optics before evaluating the coupling efficiency. The first problem arises from the fact that we cannot, in general, use the same coupling optics for imaging onto the sensor. In both cases, the aberrations corrected during the close-loop process slightly differ from those present when coupling, and a fully optimal system will require further correction, as we discuss below.

4.3.2   Evolutionary-based algorithm

We now consider further optimization of the system through evolutionary adaptation, which is the first of two blind-optimization techniques used in our setup. By design, blind techniques only have knowledge of the behavior of a system through performance metrics determined by the system output. It is our goal to correct for arbitrary wavefront aberrations, which are directly responsible for any coupling losses in our system (see Fig. 3.4). Since we can directly measure the coupling efficiency, we use coupled power as the performance metric for the RMS wavefront mismatch we wish to correct.

Although nearly any optimization strategy can be applied to blind optimization, we have opted for an evolutionary algorithm for a number of reasons. Evolutionary schemes are robust to many types optimizational landscapes, i.e., the problem need not be strictly convex, and such schemes generally converge rapidly from arbitrary starting points. Also, we can design the algorithm to allow the solution to "walk" around the optimization space, which makes it less susceptible to local maxima. The general robustness and searching abilities of evolutionary

schemes make this strategy ideal for high-dimensional and nonlinear problems such as adaptive-optic optimization. Furthermore, in studies comparing gradient and evolutionary techniques, evolutionary optimizations have been confirmed to converge faster to near-optimal settings [5]. It should be noted that the tendency of the algorithm to wander also implies that it may find the *neighborhood* of the best solution quickly, but can have difficulty locating the precise maximum within a neighborhood. For this reason, we can improve the evolutionary scheme with a final step, as described in the next section.

An evolutionary algorithm, shown schematically in Fig. 4.6 for our system, is founded on the idea of survival-of-the-fittest, which we describe here in the context of our work. With little a priori information about the behavior of the mirror or system aberrations, we choose a number of different sets of command voltages in order to initialize our algorithm. If we are continuing after close-loop operation, we can choose voltages similar to the optimal close-loop solution; otherwise, we choose voltages close to zero (i.e., close to the initial alignment conditions). Each set of command voltages is referred to as an individual within the population formed by all the sets combined. We can evaluate each individual's fitness, i.e., coupling efficiency, and rank individuals accordingly:

$$\mathbf{V^0_{pop}} = \left(\begin{array}{ccc} \mathbf{v^0_1}, & \cdots, & \mathbf{v^0_k} \end{array} \right), \text{ and } \mathbf{F^0} = \left(\begin{array}{ccc} f^0_1, & \cdots, & f^0_k \end{array} \right). \qquad (4.20)$$

In accordance with the evolutionary principle, we form a new population, giving preference to the best-fit individuals, sometimes referred to as breeding. After testing a few breeding techniques, we have implemented a purely mutation-based
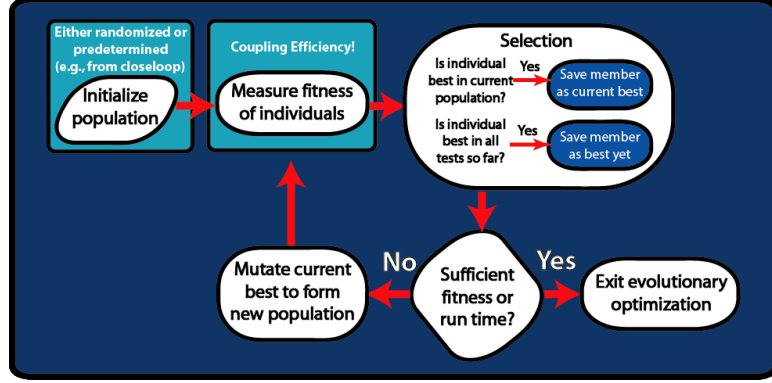
Figure 4.6: Block diagram of the evolutionary algorithm for our setup.

algorithm which renews the entire population based on the most fit individual.[1]
The mutation-based scheme effectively "shakes" the mirror around the previous
best settings, re-evaluating the fitness for each new control set:

$$\mathbf{V^1_{pop}} = \left(\begin{array}{ccc} \mathbf{v^0_1} + \delta^1_1, & \cdots, & \mathbf{v^0_1} + \delta^1_k \end{array} \right), \text{ and } \mathbf{F} = \left(\begin{array}{ccc} f^1_1, & \cdots, & f^1_k \end{array} \right). \quad (4.21)$$

As mentioned earlier, it is possible for the evolutionary behavior to cause the
population to wander away from the neighborhood of the global maximum. For
each iterative step, we keep track of the historically best-fit individuals for later
use, such that we can return to these points for better optimization. We can
choose to stop the algorithm after reaching a particular coupling efficiency, or
after a predetermined amount of time has passed. In order to fully optimize the
coupling efficiency, we exclusively use the run-time as the stopping criterion in
order to encourage the wandering nature of the algorithm. Lastly, we are currently
investigating alternative "wandering" algorithms, such as annealing and guided-
evolutionary simulated annealing (GESA) algorithms. Such schemes, especially

---

[1]It is also possible to have multiple individuals competing, either "asexually," or breeding via
chromosomal-based mixing. In the latter case, also known as genetic evolution [34], the best-fit
individuals can swap control parameters during breeding. Genetic breeding is appropriate for
when the control parameters are entirely independent, which is not typically the case in our
system.
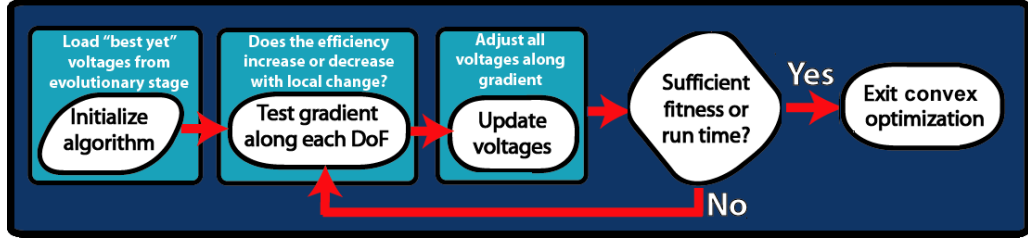
Figure 4.7: Block diagram of convex algorithm.

GESA, are very similar to evolutionary techniques and may provide an additional speed increase, as discussed in Chapter 6.

4.3.3 Convex-based algorithm

As the third and final step in our optimization process, we implement a convex-based algorithm to fully optimize the command voltages, assuming the evolutionary stage has provided a set of commands which are in the same convex-neighborhood of the global maximum. Since convergence speed in this last step is not a large concern in the performance of our system, we use a straightforward gradient-chasing algorithm as shown in Fig. 4.7.

The goal of our algorithm is to estimate the gradient of the optimization space through changes in the performance metric. Our algorithm evaluates the gradient by making small steps in each degree of freedom (DoF), and assumes that each DoF is effectively independent:

$$\mathbf{v^{i+1}} \;=\; \mathbf{v^i} + \lambda(\nabla\eta_{\mathbf{v^i}}), \text{ where} \qquad (4.22)$$

$$\nabla\eta_{\mathbf{v^i}} \;=\; \eta_{\mathbf{v^i}+\delta\mathbf{I}} - \eta_{\mathbf{v^i}}, \qquad (4.23)$$

and we have introduced δ and λ as additional control parameters; δ determines the testing step size, and λ determines the associated change to the command voltages. Note that although the assumption of independent actuators is certainly not true

in a general case, we can reduce δ until each DoF is approximately independent. Also, since we have to evaluate each degree of freedom for the mirror during every iteration, the convex algorithm is very slow compared to either the close-loop or evolutionary stages, primarily due to the mirror settling time.

This technique is similar to parallel gradient-descent algorithms, like that used by Plett et al., for fiber coupling [6, 35]; however, we have opted for a fixed step size to reduce actuator cross-talk. Similar to the evolutionary stage, we impose a fixed run time on the convex scheme. Provided that the evolutionary stage has returned an optimized position within a convex neighborhood containing the global solution, there are textbooks dedicated to the number of ways by which we could find the global maximum [36]. Our algorithm has proven effective thus far, though speed improvement remains a consideration for future implementations.

CHAPTER 5

IMPLEMENTATION OF ADAPTIVE OPTICS

5.1 Introduction

In this chapter, we describe our implementation of wavefront correction and demonstration of high Strehl-ratio adaptive optics. Wavefront correction represents the upper limit of mode correction, and we have designed our system to maximize intensity overlap in order to isolate wavefront correction. We have shown AO-limited performance of the system, which is likely the maximum achievable correction currently possible given that we have used what we believe is the best AO mirror commercially available.

5.2 Experimental Setup

Our implementation of wavefront correction can be broken down into three types of components: mode-mismatch sources, wavefront-analysis tools, and adaptive-correction elements. Our setup, pictured in Fig. 5.1, has incorporated each of these parts for maximizing wavefront correction.

5.2.1 Mode-(mis)matching

Our goal is to understand the practical limits of wavefront correction. We restrict our analysis to correcting aberrations, not apodizations, and must therefore match the intensity profiles of the coupling modes; this is accomplished by using the "free-
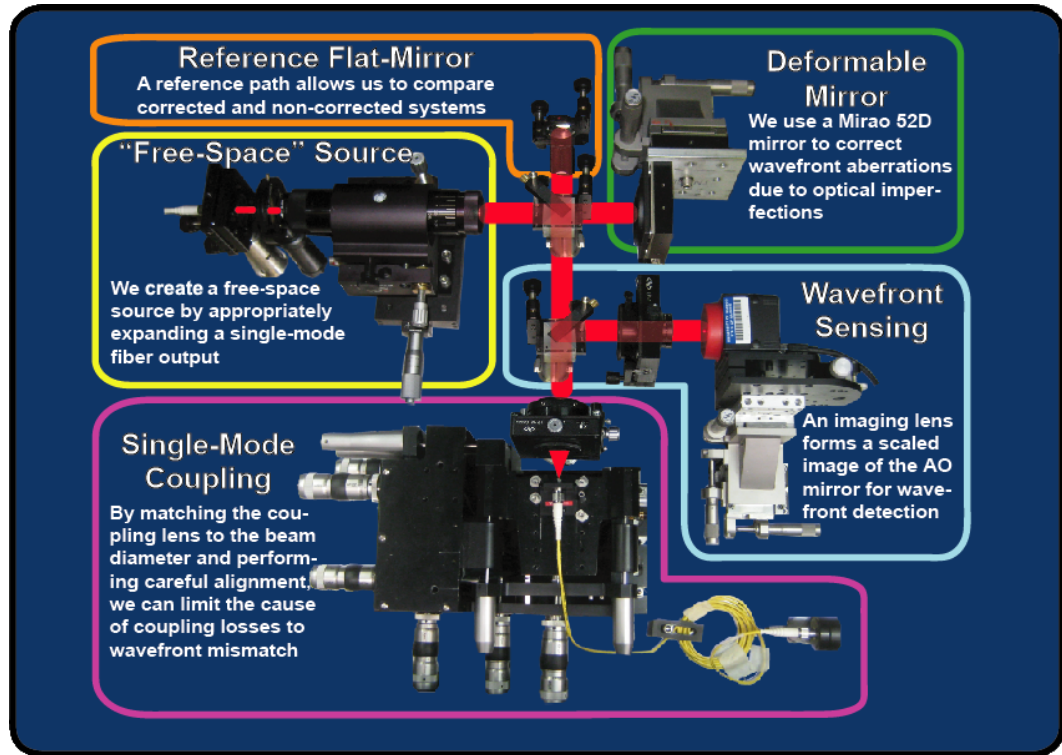
Figure 5.1: Wavefront-correction experimental layout.

space" source and single-mode coupling components shown in Fig. 5.1. Here we use single-mode fibers as the sources for the two modes to be coupled (free-space and fiber-optic), which would couple with maximum efficiency in the absence of aberrations (see Eqs. (3.17-3.19)). Although the LP_{01} mode of a fiber is not an exact mode of free space, the theoretical overlap with the optimal free-space HG_{00} mode is very high, as can be qualitatively seen by comparing Figs. 3.3 and 3.1. We have calculated that the LP_{01}/HG_{00}-mode overlap is on the order of 99.5%, though it is dependent on fiber-index properties. Considering the high calculated overlap, we assume that the LP mode is maintained throughout propagation, and that our emulated free-space mode is approximately a single mode in free space.

Despite being assured the coupling modes have similar intensity profiles, we are not guaranteed wavefront matching, due to the use of collimation, expansion, and coupling optics that will introduce aberrations into our system. These aberrations

can reduce the coupling efficiency into single-mode optics, are common among all nonideal optical systems, and are exactly what we correct for by introducing the deformable mirror. We thus have a system that matches the intensity profiles of two modes and, without adaptive optics, provides wavefront-limited performance.

5.2.2   Wavefront analysis

Perhaps as important as the correction itself, we need to be able to show that the system is working, i.e., that there are aberrations being corrected. We have three tools for testing wavefront correction: measurements of coupling efficiency, interferometry, and wavefront analysis.

Measuring the coupling efficiency can reveal the magnitude of wavefront aberrations, provided that we have optimal alignment and high efficiency (see Fig. 3.4). Our alignment techniques provide us with a reliably well-aligned system. In short, we have provided each of the optical mounts with the necessary precision and degrees of freedom to first optimize the alignment without the AO mirror. This feature is especially useful for fine-tuning the alignment of the coupling optics, since small alignment errors will induce aberrations such as coma and astigmatism.

In our system, we included two optical paths through the use of a 50:50 beam-splitter (BS), primarily to directly evaluate the impact of the AO mirror's presence, as will be discussed in the next section. An additional feature of this design is the fact that, if both paths are unblocked, we also have a Michelson interferometer with a flat mirror in one arm and the deformable mirror in the other. The fringes generated by the interferometer will reveal the surface shape of the mirror if the reference mirror is aligned on-axis (Eq. (2.18)). We thus have a method for quickly separating wavefront aberrations due to the optics from the corrections

applied by the deformable mirror itself, though this is at present only a qualitative method.

Finally, we have included an additional path in our system which allows us to sample the wavefront before, during, and after correction. As mentioned in Chapter 4, we designed the wavefront-sensing path to be removable so that we could establish the total system efficiency. Our wavefront-sensing components consist of a beamsplitter, an imaging lens, and a Shack-Hartmann sensor. Also, we match the imaging and coupling lenses whenever possible to minimize the differences in reference path. Unfortunately, we are only able to do so for focal lengths longer than 30 mm due to the housing of the SHS; for beam diameters smaller than 5 mm, we are susceptible to additional wavefront-measurement error from the difference in optical components between the reference and coupling paths.

5.2.3 AO mode-correction

The final part of our scheme for demonstrating AO correction utilizes the two mirror paths in the system. In particular, we have made use of a deformable mirror as well as a reference flat mirror to test the system with and without correction. Although we reduce our total system efficiency by a factor of four by adding the reference path, its inclusion is vital to an accurate demonstration of wavefront correction, and can be removed from the calculations via normalization. The reference mirror path allows us to characterize the coupling limitations without correction. This is an important feature of our system, since the DM itself will introduce aberrations from its unbiased state, and we must demonstrate that any uncorrectable features of the mirror are negligible compared to the inherent aberrations of the coupling optics. Without a reference path, there would be no

way to separate the aberrations introduced by the DM from those of the other optics.

More importantly, we have also included the AO correction path in our design, which provides the source of correction within our system. After experimenting with a few configurations, we settled on the normal-incidence design shown, similar to that in [5, 37], which we found performed the best under our initial testing. It is also possible to use the mirror at slight angles, which would remove the need for a beamsplitter, as discussed in Chapter 6. We could also replace the beamsplitter with a polarizing beamsplitter and quarter-wave plate combination, effectively removing the reference path without modifying the rest of the layout (see Chapter 6). In fact, one must do this to achieve absolute high coupling efficiencies. Here, where we focused on understanding the wavefront corrections, we used the simple beamsplitter.

5.3   Results

We have chosen to characterize our system based on four performance metrics: mirror utilization, command repeatability, wavefront correction and, of course, coupling efficiency. Also, we have tested several variations of our system which we will discuss here: coupling with and without ideal optics, and coupling with and without beam expansion. For near-ideal coupling optics, we used a microscope objective (MO), which only introduced minor aberrations when aligned properly (on the order of 4 nm RMS). When coupling without near-ideal optics, we utilized achromatic lenses, which introduced significantly larger aberrations depending on beam diameter, focal length, and alignment, but which have significantly higher transmission than the multielement MO.

5.3.1 Coupling efficiency

The most important aspect of our AO technique is the ability to optimize a wavefront-limited system. To truly evaluate this ability, we have considered the problem of coupling a free-space beam to a single-mode fiber, in which the free-space and fiber modes differ only by respective wavefronts (i.e., the transverse intensity profiles are *nearly* identical, as discussed at the beginning of the chapter). While the free-space mode is susceptible to aberrations during propagation, the fiber mode is determined by the quality of the cleaved and polished surface, which is reliably flat for our considerations. The coupling efficiency is therefore a direct indicator of RMS flatness as well as correction capabilities for the AO system. Since there are a number of ways to quantify AO correction, we first consider the coupling efficiency for measured power immediately before and after the coupling fiber, after dividing out reflection losses.[1] Table 5.1 provides an overview of our results for three cases: with a nearly ideal microscope objective (MO) with and without expansion, as well as with the nonideal achromats we described earlier, which use a fixed beam diameter depending on the coupling lens focal length.

We measured the coupling efficiencies with a flat mirror to distinguish what is the best possible coupling with a given set of optics, using only manual alignment and aberration balancing, from what is possible by including the DM. When testing the AO correction, we aligned all optics with normal incidence, and made no effort to balance aberrations. It is clear from our results that the starting aberrations play an important role in determining AO correction, since the inherent aberrations of the DM itself may negate any benefits. However, for systems which are appreciably wavefront-limited ($\sigma \gtrsim 20$ nm), an AO approach can improve the

---

[1]For example, we determined the Fresnel loss off each end of the fiber to be 2.3% per surface. The efficiency is then given by $\eta = \frac{P_{out}}{P_{in}} \left(\frac{1}{1-2.3\%} \right)^2$. For focal lengths shorter than 25 mm, we measured the incident power before the coupling lens and fiber, changing the efficiency to $\eta = \frac{P_{out}}{P_{in}} \left(\frac{1}{1-2.3\%} \right)^2 \left(\frac{1}{1-R_{lens}} \right)^2$.

Table 5.1: Summary of normalized efficiencies for tested configurations.

Configuration	Mirror Type	Efficiency η (%)	Change ($\Delta\sigma \approx$)	Iterations (# itr)
Beam diameter: 4 mm Coupling element: MO Optimization: Evolutionary	Flat AO	97.5 ± 0.3 97.3 ± 0.3	-0%	< 250
Beam diameter: 10 mm Coupling element: MO Optimization: Evolutionary	Flat AO	96.1 ± 0.3 97.3 ± 0.3	17%	< 2500
Beam diameter*: 6 mm Coupling element: Achromat Optimization: Evol. and convex	Flat AO	87.8 ± 0.15 96.2 ± 0.15	45%	< 5000
*Beam diameter is fixed by the focal length of the coupling optics				

system performance.

Finally, we briefly discuss the normalization considerations. We have not yet gone to great lengths to reduce all system losses, primarily since it *should be* a straightforward process to obtain antireflection (AR) coatings and wavelength-dependent components optimized for our system. The fundamental losses, or those which would appear in any version of our system, are due to Fresnel reflections off the lenses and fiber, as well as the losses (transmission and scattering) at the deformable mirror. Since one cannot easily AR-coat many multielement optics such as a microscope objective, common lenses possess a unique advantage for our system. Table 5.2 summarizes the coupling efficiencies with the current losses included, as well as the minimum coupling efficiencies expected if one includes available AR coatings for the fibers and achromat lenses (but not the MO).

Table 5.2: AO-corrected coupling efficiencies including reflection losses.

Configuration	AR Coating No/Yes	Efficiency η (%)
Beam diameter: 4 mm or 10 mm Coupling element: MO	No Yes	86.0 91.5
Beam diameter: 6 mm Coupling element: Achromat	No Yes	87.7 95.2

We have included our measured reflection losses in Table 5.2, assuming the fiber and achromats can be coated such that $R_{loss} < 0.25\%$. Despite the slightly lower normalized coupling efficiency for the achromat coupling, the potential to AR-coat the optics makes the simpler lens configuration a very attractive alternative, as can be seen in the table, with the achromat achieving the highest true coupling efficiency.

5.3.2   Wavefront correction

The ability to characterize aberrations is a fundamental necessity for illustrating wavefront correction, and we have made a number of wavefront measurements to demonstrate the successful implementation of our system. As mentioned earlier, we have evaluated AO correction in the limits of making no attempts to fill the mirror surface (beam diameter = 4 mm), as well as filling the mirror surface with negligible clipping (beam diameter = 10 mm). Figure 5.2 shows the results of our measurements, before and after running our hybrid of evolutionary and convex optimization.

For the uncorrected systems, seen in Figs. 5.2(a) and 5.2(c), we can project the wavefronts onto the Zernike basis and see that the strongest aberrations are due to coma and astigmatism (see Fig. 3.5 for example Zernike modes). The use of beam expansion also appears to introduce slight spherical aberration. These results are to be expected since we are introducing aberrations through simple lenses, as discussed in Chapter 3.4, and only the collimation optics and microscope objective are designed to compensate for spherical aberrations. As mentioned earlier, we could manually compensate for some of the coma, astigmatism, and spherical aberration through intentional misalignment of the optics; we discuss this at the end of the section.

(a) Beam diameter: 4 mm
Optimization: None.

(b) Beam diameter: 4 mm
Optimization: Evolutionary.

(c) Beam diameter: 10 mm
Optimization: None.

(d) Beam diameter: 10 mm
Optimization: Evolutionary/convex.
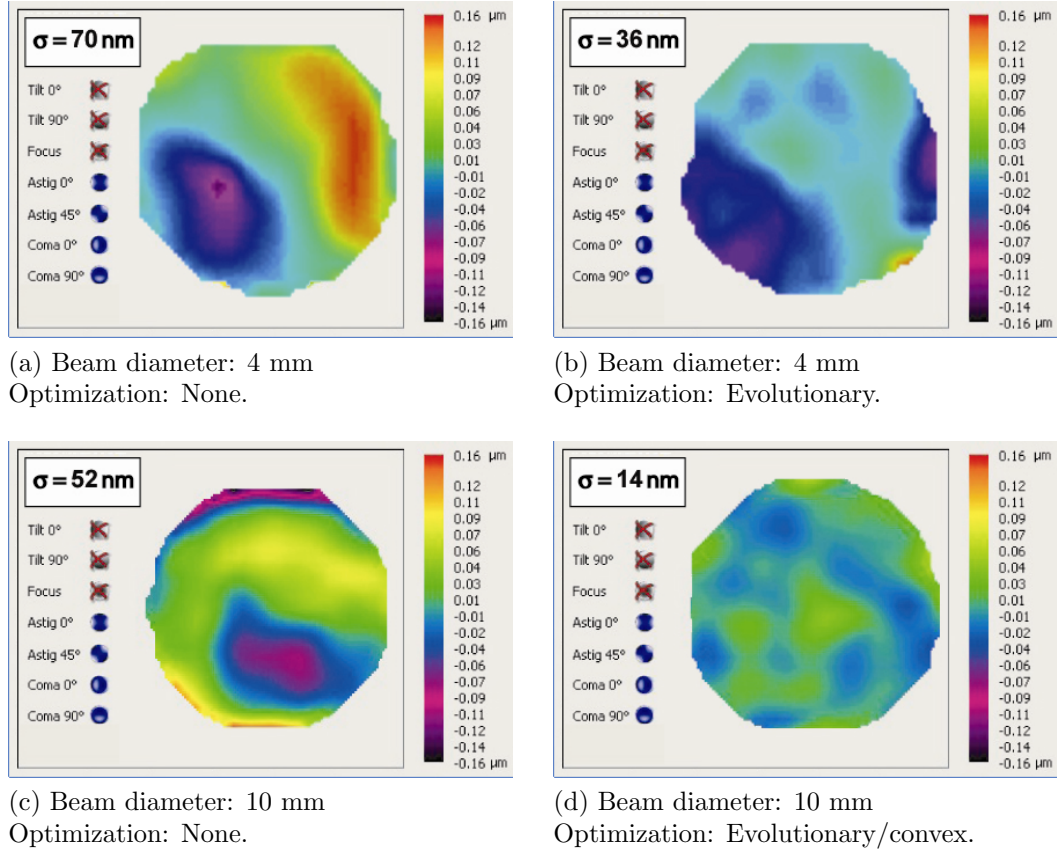
Figure 5.2: Wavefront measurements before and after correction. σ is the standard deviation of the measured wavefront.

In Figures 5.2(b) and 5.2(d), we can see a dramatic reduction in the RMS wavefronts after correction, as well as a significant difference between the systems with and without beam expansion. Again, these results confirm the intuitive expectation that using the full mirror surface provides better wavefront correction for the primary aberrations. The lack of significant spherical or higher-order aberrations in the system without expansion allows for limited correction, though the final RMS flatness is still too large for our purposes. Also, for the 4 mm beam we have assumed that there is no measurable difference between evolutionary and hybrid-evolutionary/convex optimizations: given the small number of actuators exposed, evolutionary optimization converged to what we believe is the same solution that a hybrid scheme would have attained, and without excessive run

time as might be necessary if the full mirror were to be used.

We have also observed minor disagreements between the close-loop and the blind-optimization solutions (Chapter 4.3), as shown in Fig. 5.3. The slightly different optical paths and imaging optics most likely contribute to this small difference.

(a) Beam diameter: 10 mm
Optimization: Evolutionary/Convex

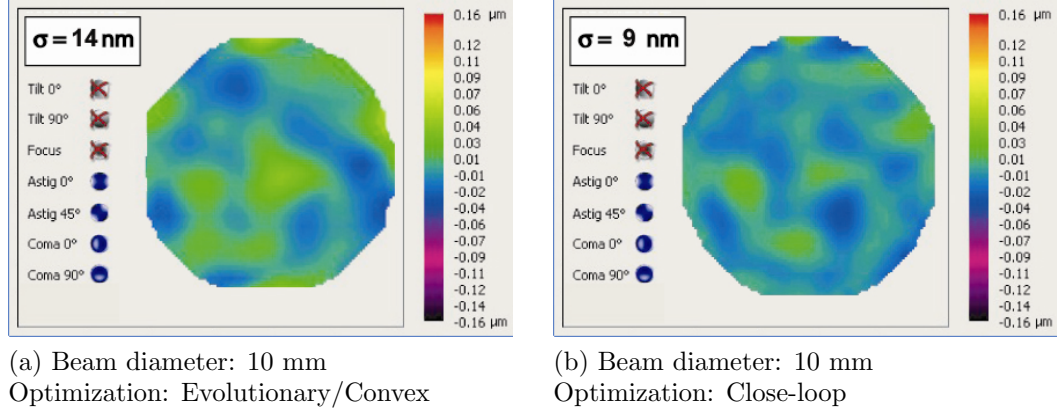(b) Beam diameter: 10 mm
Optimization: Close-loop

Figure 5.3: Comparison of blind-optimization and close-loop solutions.

Despite the seemingly better solution through close-loop, we have consistently observed better coupling efficiency via blind optimization. However, the close-loop process is significantly faster than blind optimization, as discussed in Chapters 2 and 4, making it an ideal starting point for our evolutionary and convex schemes. We have tested this three-step process of close-loop, evolutionary, and convex optimization, and found it to perform as well as or better than any combination of the individual algorithms with respect to coupling efficiency.

Lastly, we have found the DM to perform within its 10-nm RMS flatness specification, though not by much. Typical settled solutions range from 9-nm to 25-nm RMS flatness after correction, with the flatness largely dependent on the magnitude of correction needed. The RMS flatness sets the upper limit on the performance of the system under ideal conditions, as shown in Chapter 3, and we can only correct an arbitrary wavefront to within 10-nm RMS at best.

If the system is already close to this point, there is little to be gained from AO correction, as illustrated in Fig. 5.4 for a system for which most of the aberrations present could be removed via aberration balancing before any AO correction.

(a) Beam diameter: 10 mm
Optimization: None (manual balancing)

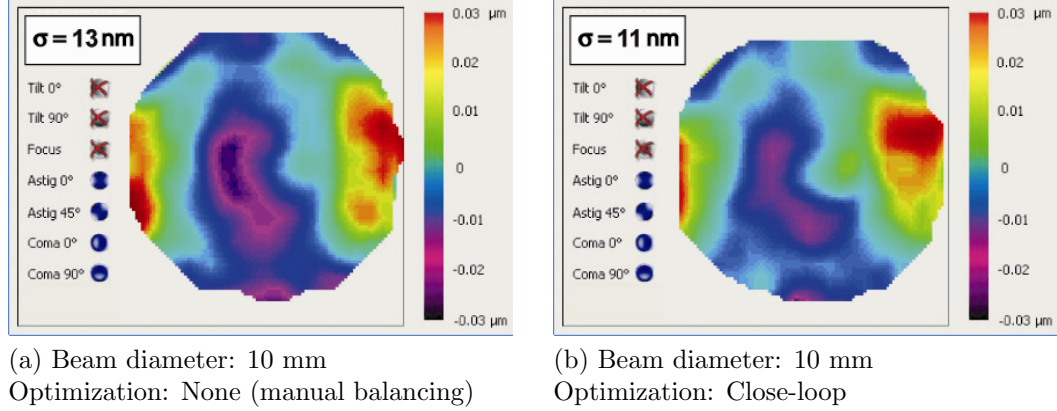(b) Beam diameter: 10 mm
Optimization: Close-loop

Figure 5.4: Wavefront correction near the performance limit of the DM.

5.3.3   Mirror utilization

In order to make optimal use of our system, it is necessary to make optimal use of the deformable mirror. Since we are dealing with a system limited by the amplitude-weighted RMS wavefront-mismatch (see Eq. (3.26)), it would seem that we should concentrate on correcting the highest intensity region of the beam. However, we must avoid introducing apodizations due to clipping once we fill the aperture of the mirror; such efforts reduce the coupling efficiency according to Eq. (3.17). We have studied the coupling properties over the range from "no expansion" to the limit of maximal expansion without measurable clipping, i.e., from a beam diameter of 4 mm to 10 mm. At the smallest and largest diameters we have 99% of the incident power filling 16% and 100% of the 15-mm diameter mirror aperture, respectively.

For the two limits of surface utilization we observed different results depending on the coupling optics. First, when using the MO, we found that using the entire

DM surface provided no measurable advantage over the system without beam expansion. In essence, we observed that the largest aberrations present without beam expansion were of low order (coma/astigmatism) and could be corrected using only a small portion of the mirror surface. The addition of beam expansion in this case actually *added* higher-order aberrations, which were subsequently corrected for by the mirror. If we used irises to reduce the beam diameter and normalized the coupling efficiency according to Eq. (3.17), thereby including the aberrations due to the expansion optics without the full use of the mirror, we observed the expected drop in coupling efficiency (see Fig. 5.5).
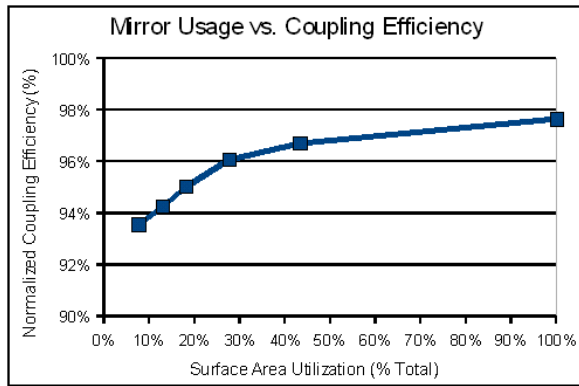
Figure 5.5: Normalized coupling efficiency dependence on DM-surface usage. The surface utilization is defined as the ratio of the area of the beam, taken at the 99% power level ($A_{beam} = \pi(1.5w_0)^2$), to the area of the mirror aperture ($A_{DM} = \pi(7.5 \text{ mm})^2$).

When using achromats for coupling, we observed a large difference in the system efficiency with and without expansion. In this situation, the coupling lens introduced aberrations that were larger and higher-order than those of the collimating lenses, and that only the system with beam expansion could correct for. In our system, the collimation optics set the beam diameter out of the free-space source, while the coupling optics focus the free-space beam onto the surface of another fiber. Although the mirror can still largely correct for simple aberrations, such as astigmatism and coma, terms higher order than coma require

a higher spatial-frequency resolution than small sections of the surface can provide.

An additional consideration when filling the mirror aperture arises from the inherent aberrations AO mirrors have due to the actuator patterns. For low surface-area usage, these inherent aberrations have lower spatial frequencies compared to the aberrated wavefront, and may resemble the primary aberrations discussed in Section 3.4.2. The primary aberrations can be largely corrected by balancing lens alignments, reducing the standard deviation by as much as a factor of two [21], and subsequently making the mirror surface effects less apparent. When the mirror aperture is filled, however, the inherent AO aberrations will be of a higher order, and will not be able to be balanced by any simple optical tricks. If these higher spatial-frequency aberrations are too large, beam expansion begins to degrade the coupling efficiency. Further discussion of this issue is provided in Appendix A, complete with our own experiences.

5.3.4   Actuator repeatability

Next, we consider the ability of our system to converge toward a global maximum via metric-based optimization of coupled power-stability. We tested for actuator repeatability by performing 10 identical trials, and calculating the command-voltage standard deviation over the 10 trials for each actuator. We evaluated four cases: evolutionary optimization with no beam expansion, evolutionary and convex optimization with beam expansion, convex optimization with beam expansion, as well as evolutionary and convex optimization with beam expansion after starting from a previously settled solution.

We found what we largely expected to find: the standard deviation of the settled actuator voltages is inversely dependent on the intensity of the field illuminating that actuator. In Fig. 5.6, we have plotted the inverse of the stan-

dard deviation to emphasize the best performing regions; we also noted the mean standard deviation across all actuators. We have calculated the ideal RMS to be on the order of 0.5 mV, which we calculated by comparing the ratio of expected RMS flatness and total actuator stroke to the total input voltage range ($\sigma_{v_{act}} \approx \frac{10 \text{ nm}}{50 \text{ } \mu\text{m}} \times 2 \text{ V}$). The mean standard deviation decreases significantly when adding beam expansion. Furthermore, if we exclusively use our convex optimization algorithm, the standard deviation is again reduced. If we begin optimization from a previously obtained maximum, the standard deviation drops dramatically, and a few actuators approach the ideal RMS limit.

Although important for demonstrating a consistent solution, actuator repeatability is not a sufficient criterion for an optimized system. For example, both Figs. 5.6(c) and 5.6(d) indicate better repeatability than Figs. 5.6(a) and 5.6(b), yet we measured the coupling efficiencies associated with the convex algorithm data to be notably worse than the evolutionary algorithm (90% compared to 94%), while the efficiencies associated with the algorithm picking up from a local max were notably better (97% compared to 94%). Rather than associating repeatability with wavefront correction, we use it as an indicator of both algorithm behavior and optimization landscape. We conclude that the similarity between Figs. 5.6(b) and 5.6(c) indicates a partially convex optimization space, while the significant difference between Figs. 5.6(b) and 5.6(d) indicates a number of local maxima near the optimal solution. From the lower mean standard deviation, we conclude that the convex algorithm is more consistent than the evolutionary scheme. Aside from noise in the system (e.g., mechanical motion or power drift), a convex algorithm should follow an identical convergence path if run multiple times, and should therefore be the closest to the estimated ideal-RMS voltage deviation. The fact that our tests show the convex scheme to be less than perfectly repeatable implies that there must be sources of noise in the system which impact the optimization
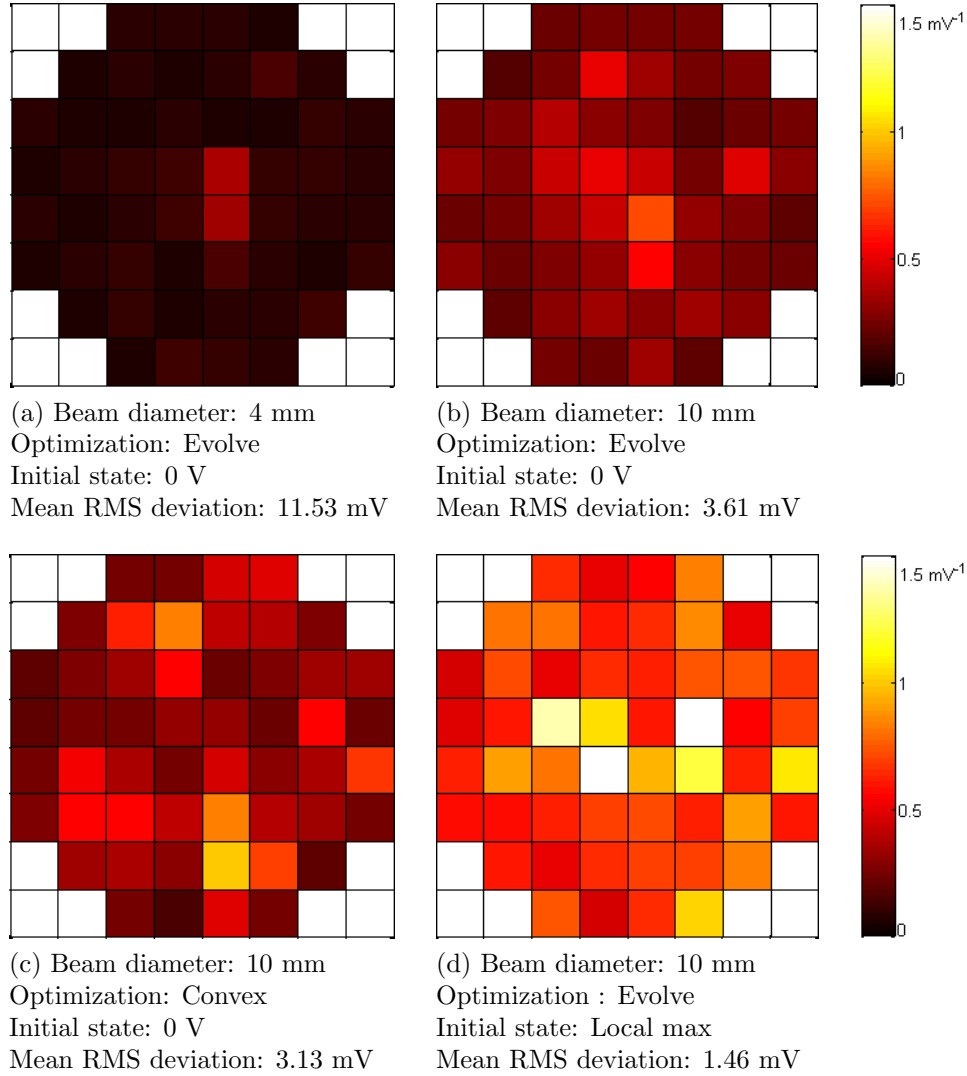
(a) Beam diameter: 4 mm
Optimization: Evolve
Initial state: 0 V
Mean RMS deviation: 11.53 mV

(b) Beam diameter: 10 mm
Optimization: Evolve
Initial state: 0 V
Mean RMS deviation: 3.61 mV

(c) Beam diameter: 10 mm
Optimization: Convex
Initial state: 0 V
Mean RMS deviation: 3.13 mV

(d) Beam diameter: 10 mm
Optimization : Evolve
Initial state: Local max
Mean RMS deviation: 1.46 mV

Figure 5.6: Actuator-repeatability results (inverse RMS deviation, σ^{-1}).

metric on a time scale comparable to a single algorithm iteration.

We have identified a few potential sources of error that could degrade the actuator-RMS performance, i.e., fluctuations in the source power, slight mechanical drift within the system, or degenerate wavefront solutions due to piston motion. Although we have observed power issues in the past, we have since insulated the source to minimize these issues, as well as included "double-checking" features within the algorithm to compensate for the remaining drift. We do not consider power fluctuations to be a limiting factor for evolutionary optimization due to

competition within the algorithm. However, small errors in estimating a convex gradient could have a lingering effect on subsequent estimates until the error is corrected. Next, we have observed mechanical drift responsible for an efficiency drop of less than 10% by measuring the efficiency of an uncorrected system immediately after alignment and monitoring the coupling efficiency over time. We can limit these errors (usually to less than 2% per day) by providing an initial settling time before running any optimization. Some of the actuator variation could also be attributed to the partial insensitivity of the mirror shape to piston motion, that is, the movement of the entire mirror surface along the optical axis. Luckily, the issues with mechanical motion and piston do not impact the coupling efficiency or wavefront correction.

CHAPTER 6

CONCLUSIONS AND OUTLOOK

6.1 Conclusions

Not long ago, it would have been counterproductive to utilize adaptive optics for high-Strehl-ratio (SR) systems at visible wavelengths; the inherent aberrations would have resulted in losses greater than the potential improvement. Although adaptive optics have been in use for a number of years for astronomy and large-aperture/long-wavelength systems, the technology has only recently progressed to the point where nanometer-scale features can be reliably corrected. To the best of our knowledge, this work represents the highest efficiency and lowest RMS flatness obtained to date for single-mode coupling via adaptive optics with visible light.

6.2 Modifications and Possibilities

There are still a number of modifications mentioned throughout this work which could extend the capabilities of our AO system. We have begun work toward some of these goals, while others are simply ideas for improvements or applications.

6.2.1 Implementation

We begin with a discussion of the improvements we could apply without major experimental-layout changes. There are two primary weaknesses of our approach

as described: a reduced total system efficiency due to preventable losses, and the algorithmic-convergence speed. The Fresnel reflection losses, and inclusion of a reference path, are the largest factors reducing the total efficiency. We have found multiple sources in industry able to provide AR-coatings to counter reflection losses at a desired wavelength, all with lower than 0.25% reflection loss per surface. It is also possible to improve the coating on the mirror itself (which at present has a reflectivity of better than 98% at 655 nm as shown in Fig. 4.4), although it would be a more difficult and customized process.

Next, we could remove the reference path without significantly altering our experimental layout, potentially increasing the total system efficiency by a factor of four. If we restrict the input to horizontally polarized modes, we can increase the efficiency by replacing the 50:50 beamsplitter with a polarizing beamsplitter (PBS) followed by a quarter-wave plate (QWP) as shown in Fig. 6.1.
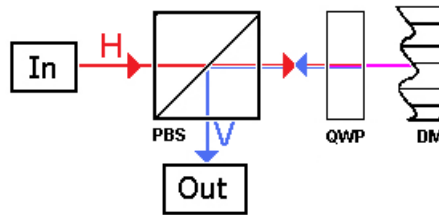

Figure 6.1: Proposed PBS and QWP modification.

With this setup, the horizontally polarized input mode would be transmitted through the PBS, rotated to vertical polarization after a double-pass through the QWP, and reflected on the second pass through the PBS. Equivalently, we could use vertically polarized light by using the reflected arm of the PBS. If we incorporate low-loss AR coatings and polarization optics, the total-system efficiency would be limited only by the quality of the PBS. With currently available PBSs, for example, the efficiency limit would be better than 95% for a typical cube-PBS, and could be higher depending on wavelength and PBS quality (e.g.,

a Brewster-angle PBS allow efficiencies above 99%).

Another alternative, pictured in Fig. 6.2, allows for high-efficiency correction and relaxes the polarization restriction, is a modification of a standard tilted-mirror layout, and is similar to that used by Zhu et al. in [38] to generate Zernike modes with a deformable mirror.
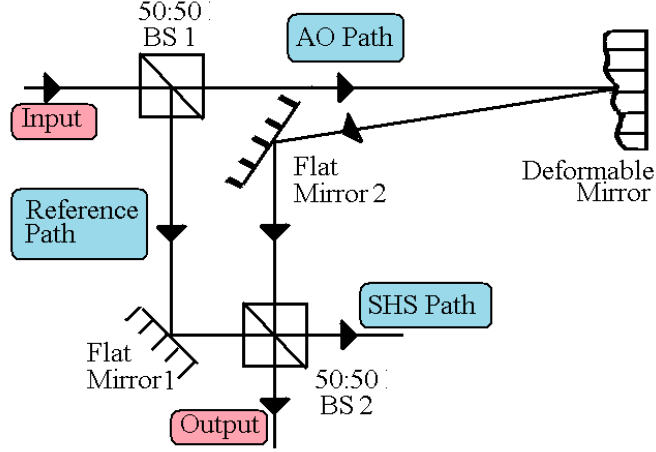

Figure 6.2: Proposed tilted-mirror scheme.

The addition of two beamsplitters provides a reference path that is very useful for evaluating the performance of the system without any AO, similar to our current design. Unlike our current setup, however, we can entirely remove the beasmplitters (and the reference path) in order to evaluate the total system efficiency with AO. Unfortunately, this design also balances the effective area of the DM aperture with the required path lengths; e.g., when closer to normal incidence, the mirror aperture appears mostly circular, but the DM must be positioned further from the "flat mirror 2" to separate the input and corrected beams. Shorter path lengths will reduce both the system sensitivity to mechanical vibrations as well as aberration propagation (into intensity fluctuations). We suspect that the impact of the slightly elliptical mirror aperture on a Gaussian mode may be minimal compared to the benefits of a simpler setup with fewer optical components

and no inherent polarization dependence, and we are considering this layout for future work.

Another modification we have considered is changing the evolutionary stage of our correction algorithm. In particular, we are interested in evaluating the performance of simulated-annealing (SA) [39] and guided-evolutionary-simulated-annealing (GESA) [40] algorithms. Both algorithms are similar to evolutionary optimization, but have a few distinct features which change the overall behavior.

Briefly, SA was designed to model the annealing process in crystalline materials in which an ensemble of atoms is formed into a high-quality crystal through slow heating and cooling. To model this process, we begin with an ensemble of points in an optimization space, each representing a set of commands for a particular system, and each assigned a cost function according to a chosen metric. The algorithm perturbs each point, and re-evaluates the cost for the new set of commands. Unlike evolutionary optimization, which would only move toward a lower cost, SA has an additional "temperature" parameter which introduces randomness into the decision making: the new point is accepted if the cost is lower, and also has a chance of being accepted if the cost is higher. As the system "cools," the chance of accepting a higher cost decreases. This behavior allows the algorithm to escape local maxima easily when the temperature is high, and encourages the algorithm to concentrate all the testing points near the global-minimum cost.

The GESA approach is a straightforward modification of SA, which also incorporates aspects of evolutionary control. Rather than concentrating on a large ensemble of points, GESA works by running multiple, competing SA processes. The weighted cost of each competing SA process becomes the performance metric for evolutionary optimization, where the size of each SA ensemble is determined by its overall success relative to the other processes. A GESA algorithm shares many of the benefits of SA algorithms, such as the resistance to local extrema,

66

and is additionally capable of exploring many regions of the optimization space while prioritizing the best-performing regions.

6.2.2 Mode conversion

Another possible application of wavefront correction is as part of an efficient and dynamic mode converter, i.e., a device which can simultaneously reshape both the intensity and phase of an incident mode with minimal loss. We suspect that we can exclusively use wavefront corrections as a building block for performing general mode conversion. This is certainly true for a subset of problems, e.g., beam expansion (Fig. 4.1). Here we discuss one potential realization of this idea, in which we wish to be able to emulate mode-conversion systems using adaptive optics. We can implement an AO-mirror mode conversion using the aforementioned PBS/QWP technique and two deformable mirrors, as shown in Fig. 6.3.
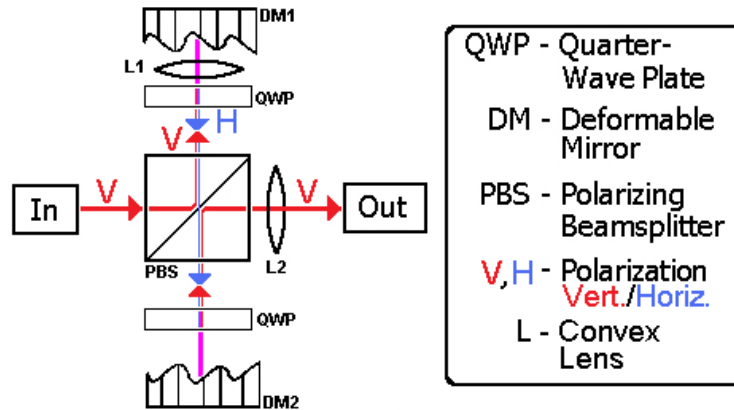

Figure 6.3: Potential two-mirror mode-conversion scheme.

As drawn, we can modify the input mode's wavefront using DM1, focus the mode with L1, modify the focused wavefront using DM2, and collimate the output mode via L2. Aberrations added at DM1 will change the intensity and wavefront at DM2, and aberrations added at DM2 will change the intensity and wavefront

at L2; consequently, the output mode is dependent on both mirrors. We are interested in the case where the output remains unchanged if the DMs are flat, which requires that L1 and L2 form a 4f-type imaging system as described in Chapter 4. Also, if we assume that the separation between DM1 and L1 is much smaller than the focal length of L1, then the effective lens formed by passing through L1 twice, which we will denote L1', has a focal length approximately equivalent to half the focal length of L1 under the thin-lens approximation [12]. Although an ideal DM would be able to directly produce the necessary focus (removing the need for any lenses), the large deformations required for any magnification could quickly lead to actuator saturation, reducing the correction quality.

By designing the layout such that L1' is exactly at DM1 and L2 is away from DM2, we have introduced a convenient way to separate the effects of each DM on the output mode specifically. If we place both L1' and L2 one focal length away from DM2, the modes at each of the lenses will be in the focal plane at the surface of DM2. By design, the output of our mode converter should match the target mode at L2, and since nothing alters the mode after DM2, the *focused* output mode should also match the *focused* target mode at DM2. The second mirror can only correct the wavefront at DM2, however, so we must have matching intensity distributions without any contribution from DM2. We can therefore separate our mode-conversion scheme into two components: intensity correction with DM1, and wavefront correction with DM2.

Lastly, it is possible to simulate this system by utilizing the Fourier transform, which is an approximation for paraxial fields focused by spherical lenses [9]. We have performed some preliminary simulations using MATLAB and the fast Fourier transform (FFT), as well as evolutionary optimization of the mirror settings, and have observed promising initial results (Fig. 6.4). In particular, we have seen very high overlap for performing a relatively simple correction from a Gaussian mode

to a steeper-edged squarelike mode (similar to a square waveguide mode), which began with an overlap close to 70%.

(a) Input field magnitude (b) Output field magnitude (c) Target field magnitude
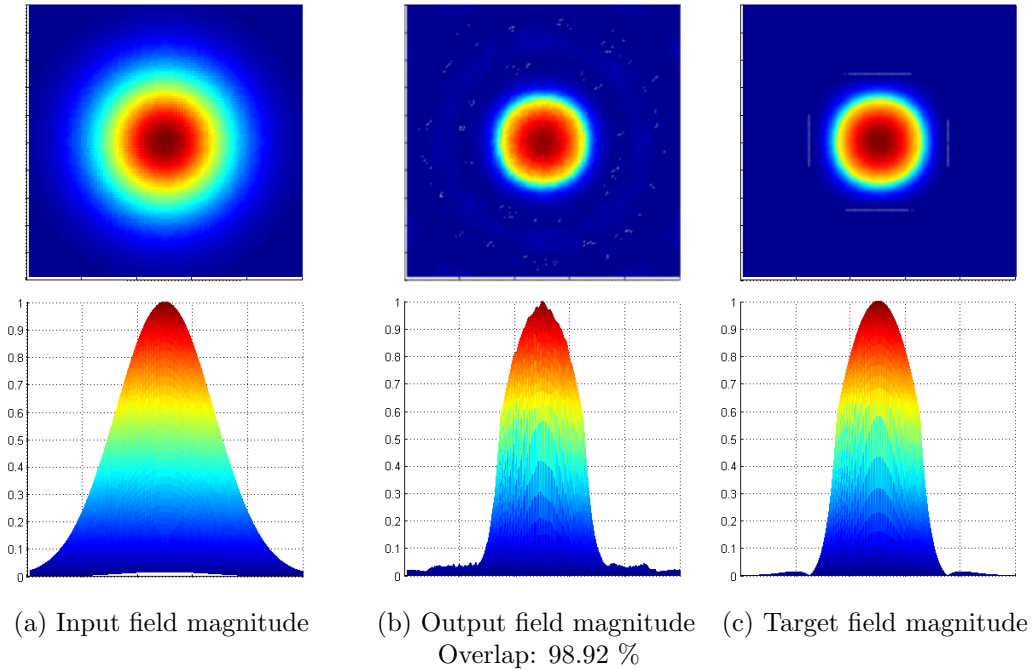Overlap: 98.92 %

Figure 6.4: Initial two-mirror mode-conversion results.

In this first test, we allowed for perfect wavefront control at each point, which would certainly be limited by the actuator density on real DMs. We are continuing to develop practical simulations, as well as working to develop a rigorous theoretical formulation for determining the optimal mirror settings. After the above corrections, our net mode-coupling efficiency is limited by the desired correction and the spatial resolution of each DM, which will ultimately determine how efficiently we can perform correction for two particular modes.

APPENDIX A

DIAGNOSING A DEFORMED MIRROR

A.1 Introduction

In this appendix we outline a number of problems we have encountered with our
deformable mirror system during the past two years, as well as the methods we
have used to test for each. These problems include beyond-tolerance aberrations,
power-supply failure, and mirror settling times. Some of these problems may be
compensated for, while others require repairs or replacements.

A.2 Beyond-Tolerance Residual Aberrations

Despite the superior performance of our AO mirror when compared to others
commercially available (see Chapter 4), we found that our first mirror from Imag-
ine Optic was unable to meet its specified tolerance for RMS flatness. While the
manufacturer specifications state that the mirror can obtain better than 10-nm
RMS flatness, the best we found it could obtain was closer to 20 nm, which un-
acceptably limited the system performance. Our investigation determined that
these aberrations were very likely due to the actuators attached to the mirror
surface.

A.2.1 Symptoms

There were a few clear indicators that the residual aberrations were due to the deformable mirror. First, it appeared that high spatial frequencies were caused by the actuators, diverged quickly upon propagation, and created a distinct intensity pattern on the output mode after a short propagation distance. This intensity pattern was constant regardless of the mirror settings, including after close-loop and blind-optimization correction. Also, the pattern moved with respect to the mirror, i.e., a vertical or horizontal translation resulted in a corresponding movement of the pattern on the output mode. Since such a pattern was visible, we suspected that it was possible the inherent aberrations of the deformable mirror were beyond its specified tolerance. We observed such a pattern forming in as little as 25 cm after reflecting off the DM, whereas there was no noticeable pattern when using a flat mirror (Fig. A.1).

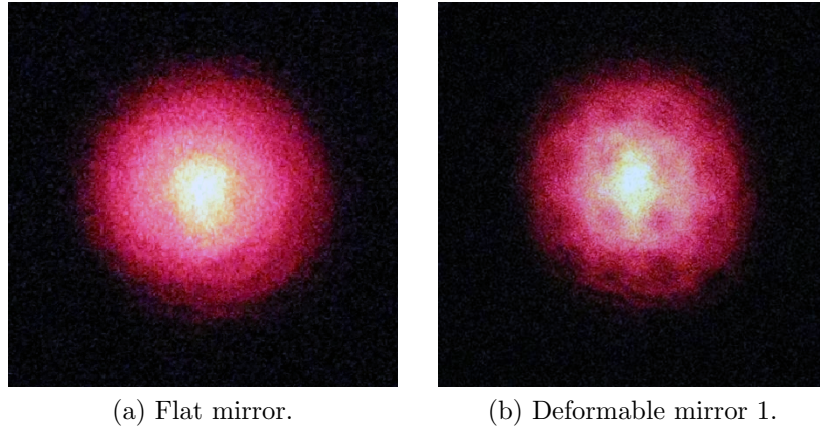(a) Flat mirror.   (b) Deformable mirror 1.

Figure A.1: Output intensity patterns with and without the deformable mirror present (beam diameter: 10 mm).

An additional symptom of RMS-aberration problems was a failure of the system to obtain its specified flatness via close-loop correction. Many factors could impact the close-loop process, and a carefully aligned and properly imaged system was necessary for the best results. Since the residual RMS flatness after

correction was always larger than the specified tolerance, the mirror unit again appeared to be out-of-spec for RMS flatness. Although the close-loop flatness would be sufficient for demonstrating that the system was operating within its specifications, it was *not* sufficient for showing it was beyond its specified limits because of contributions from the rest of the optics. However, when there were reasonably low aberrations due to the optical system compared to the DM, as checked by replacing the DM with a flat mirror, we interpreted the residual aberrations after close-loop correction as an indicatior of the aberrations due to the mirror, and concluded it warranted further investigation.

A.2.2 Diagnosis

It was necessary to measure surface shapes in order to conclusively detect any residual aberrations due to the mirror, for which a number of techniques are commonly used. We opted for interferometric testing, similar to the methods mentioned in Chapter 2, which was well suited for noncontact and large-aperture surface measurements.

We evaluated the mirror surface with a Veeco NT1000 interferometric surface profiler, which could be set to use either vertical- or phase-shift interferometry (VSI or PSI). VSI utilizes white-light interferometry, where interference fringes are visible only over a very short and well-defined distance due to the short coherence length of a broadband source. The surface is translated through this region in a Michelson-type interferometer, and the shape can be reconstructed from the placement of high-contrast fringes, much like the contours of a topographical map. For PSI, quasi-monochromatic light is used in the same interferometer, only now the surface shape can be reconstructed from the interference relationships in Eq. (2.18). Both methods possess advantages and disadvantages, with VSI more

robust to surface discontinuities and reliable for large features, and PSI more robust to vibrational noise and reliable for subwavelength features.

After noticing a few symptoms of residual aberrations, we had a cross-section of the mirror surface measured through VSI in overlapping, 1-mm^2 sections (the largest area possible with the available equipment), which we pieced together. After removing tip, tilt, focus, and the noisy artifacts due to the measurement and reconstruction process, we found that the mirror surface was covered in bumps 50-80 nm in height (see Fig. A.2).
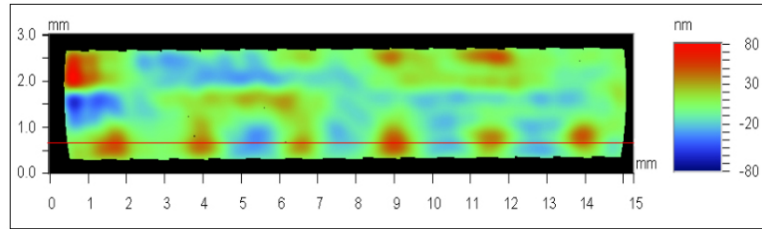
(a) Deformable mirror surface profile.
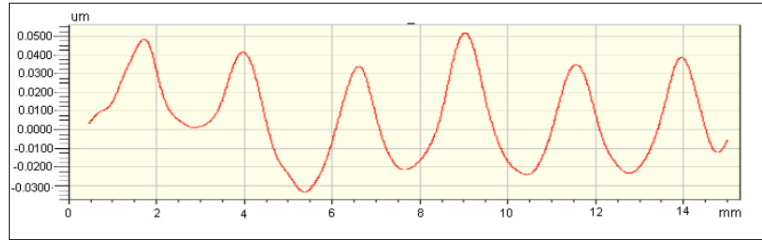
(b) Slice of surface profile along the solid red line

Figure A.2: VSI surface profiler scans of our initial deformable mirror.

The positions of the bumps corresponded to each of the actuators across the mirror surface. Unfortunately, we had to perform these measurements with an inactive mirror due to equipment restrictions in the cleanroom facilities which provided the Veeco system. As such, each of the scans was taken with the mirror in an unbiased state, rather than a zero-volt or actively flattened state. Without any active tension other than from the weight of the mirror surface, there appeared to be a 19-nm RMS aberration inherent to the mirror surface, which was in agreement with our initial suspicions, and would prevent the mirror from ever obtaining its

specified flatness.

A.2.3   Correction

To the best of our knowledge, there is nothing that can be done to correct the mechanical limitations of the mirror other than replacement. After our diagnosis and demonstration of the problem to Imagine Optic, we were eventually able to get our first mirror replaced. We repeated our previous tests on the replacement DM, as shown in Figs. A.3 and A.4 for both mirrors.

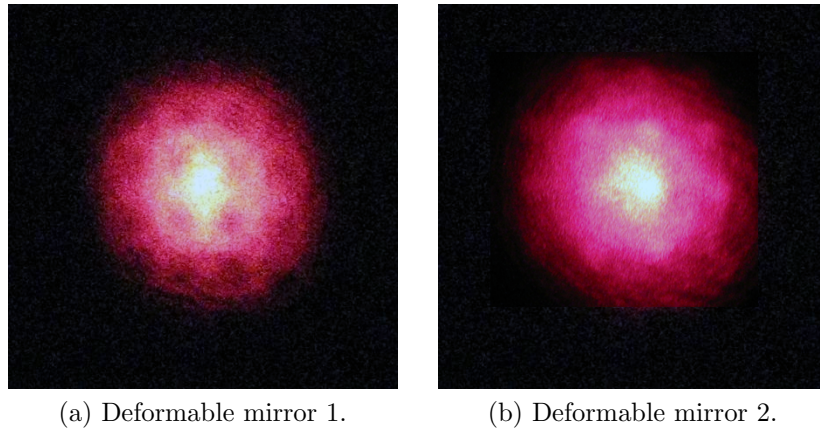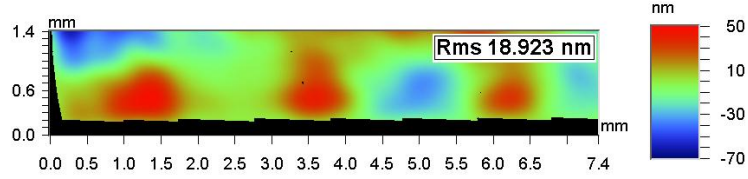(a) Deformable mirror 1.   (b) Deformable mirror 2.

Figure A.3: Output intensity patterns with the initial and replacement mirrors (beam diameter: 10 mm).

As a first test, the intensity pattern observed after reflecting off the replacement mirror was less noticeable than before, although it was still present. We also tested the surface shape of the replacement using the Veeco system, and found a measurable improvement in the scale of the RMS aberrations (note the RMS values and lighter colors in Fig. A.4(b) when compared to Fig. A.4(a)). After testing the inactive mirror, we ran the new mirror in a close-loop experiment and very quickly observed better than 10-nm RMS flatness after correction, providing the necessary confirmation that the new mirror was operating within its specifications.

(a) Deformable mirror 1 surface-profile section (taken with VSI).
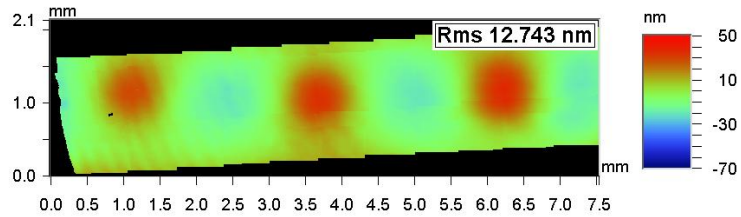
(b) Deformable mirror 2 surface-profile section (taken with PSI).

Figure A.4: Comparable sections of surface-profile scans for the original and replacement mirrors.

As noted in Fig. A.4, we used VSI for our initial scans and PSI for our follow-up scans. After evaluating the first mirror, we found that the scale of the aberrations were more appropriate for PSI than VSI, and that the moving parts involved in VSI introduced nm-scale errors. We also determined that averaging 5-10 VSI scans greatly reduced these errors, and that our original scans, each of which was an average over four scans, were sufficiently accurate for stating the mirror was beyond its specifications. Although our preference was to perform a side-by-side comparison of the original and replacement mirrors, Imagine Optic was unable to allow us to have both simultaneously.

A.3 Power-Supply Failure

During our testing of the AO system, we ran into an unexpected shutdown problem when driving the mirror with large average command voltages. Since there is no direct feedback from the mirror or mirror power supply, this problem was only

apparent when monitoring the output of a corrected system, and resulted in a complete, albeit temporary, failure of the system. Although this problem was not outlined in the operation manual when we received our system, it has since been included in updated versions. At the time of this writing, the specifications now state that the absolute sum of the applied voltages must be less than 25 V, which we have found still to be insufficient.

A.3.1   Symptoms

Once we were aware that a temporary failure of the AO mirror was possible, such an event was somewhat obvious. The power supply would shut down the mirror for a period of time, accompanied by an audible "click," and the mirror would revert to its unbiased state. At some later time, the supply turned the mirror back on, and the system continued as if the mirror had been active the entire time. If the system was attempting to optimize the mirror shape during the inactive time, it would walk randomly according to performance-metric fluctuations. If the mirror was maintaining a constant shape for coupling, the power would drop suddenly, maintain its inactive level, and periodically repeat this cycle (see Fig. A.5).
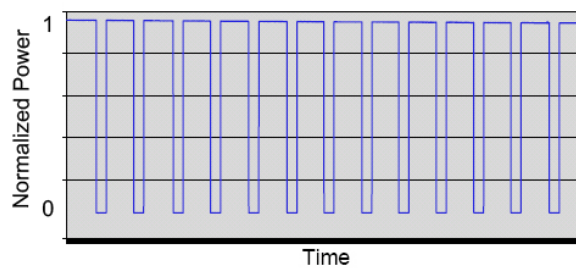

Figure A.5: Measured trend illustrating the periodic shutdown of AO system.

A.3.2 Diagnosis

The shutdown problem was straightforward to conclusively evaluate, and it was further possible to approximately predict the shutdown according to the average applied input voltages. We found it very convenient to use of the inactive state of the mirror as the initial position in a coupling system, and to use the active state to apply a variable tilt to the mirror. In this setup, there is no coupling unless the mirror has failed due to the tilt, and we can measure the characteristics of the shutdown problem over time for different magnitude tilts (see Fig. A.6).
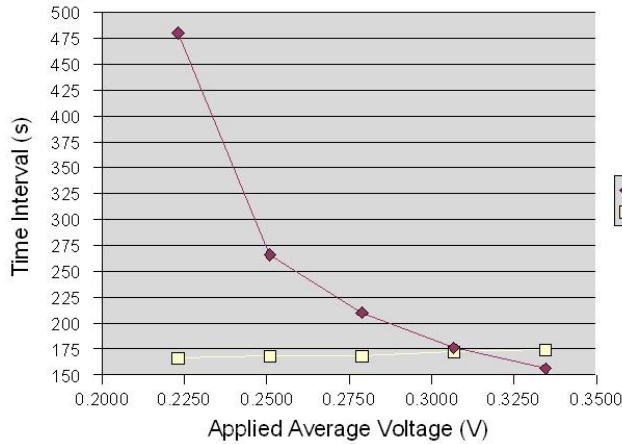
Figure A.6: Characteristic failure of the power-supply under varying applied voltages.

For average applied voltages less than 225 mV per actuator (absolute sum of less than 12 V), the mirror did not shut down. Above this threshold, the mirror shut down after increasingly short periods of time. The inactive time was nearly constant for each of the tested settings.

A.3.3 Correction

We concluded that these results indicated an overheating problem with the power supply or mirror, which would require repair, replacement, or total avoidance. For

an overheating issue, increasing the power consumption would cause an increase in operating temperatures, eventually reaching a predetermined shutdown threshold. After a temperature-threshold shutdown, the inactive system would cool and reactivate. If the threshold temperature was fixed, the time until shutdown would depend on the power consumption, while the time after shutdown would be fixed by the threshold conditions. Similar behavior would be observed if the power supply monitored power consumption; shutting down for a fixed time after reaching a given threshold (e.g., via a slow-reset fuse).

After discussing the problem with Imagine Optic, we were able to test an additional power supply, which we measured to fail at even worse voltages, as low as an absolute sum of 7.5 V! Although we would like to try the recently released upgrade supply, our discussions with the company are at a standstill. For the time being, unfortunately, we are left having to avoid this problem rather than correct it. This has not been a problem for wavefront correction, where the absolute sum of actuator voltages is typically below 2.5 V, but may become problematic in larger-stroke applications, i.e., total wavefront and intensity conversion.

A.4   Settling Time

One type of subtle error which appeared in our AO system was associated with the repetition rate (rep-rate) at which the DM was able to properly function. According to the Mirao52D user guide, the mirror was capable of rep-rates of up to 200 Hz. We found this to be misleading for two reasons: the acquisition rate was typically lower than 20 Hz when operating with the Casao software suite, and the mirror settling time appeared to be largely dependent on both the required accuracy and command-voltage variance. Given the large dynamic range of the mirror (± 50-μm deformation), we suspected that our application requirements,

i.e., less than 10-nm RMS error, were beyond the typical accuracy requirements used for this specification.

This discrepancy needed to be compensated for, and caused problems when evaluating mirror performance faster than it could respond to, especially when making optimization decisions below the 1% level. For repeated measurements of a control signal applied to the mirror, we found the RMS deviation of the coupling efficiency only to be lower than 1% when limited to rep-rates of 3-20 Hz, as described below.

A.4.1 Symptoms

Problems associated with the rep-rate were not always easily apparent, and varied based on the coupling efficiency and amount of change between command voltages. For our blind-optimization coupling system, the transient behavior of the mirror introduced uncertainty into the efficiency measurements since the state of the mirror could change from the time of measurement to settling. If the set time of the mirror, i.e., the time between applying commands and measuring the outcome, was less than the settling time of the mirror, the uncertainty of each measurement could limit the system performance.

If the system was limited by settling times, it would ultimately fail to converge to the highest possible efficiency. Although this is a vague statement, we have observed this behavior in the form of anything from immediate divergence, to lack of convergence, to simply mediocre performance, making it difficult to be more specific. Since there were many factors that could cause poor performance, a better indicator of a settling-time problem was a performance improvement when the set time was increased, which required a minimum of two trials to observe.

A.4.2 Diagnosis

The easiest method we developed for determining the mirror settling was to apply noisy sets of command voltages followed by a control set of command voltages, and to measure the coupling efficiency each time the control set was applied. By varying the DM set time and the magnitude of the applied noise between control sets, we could determine the optimal settings for the DM rep-rate.

First, we chose the solution of a coupling experiment under typical operating conditions (beam diameter: 10 mm, $\eta \geq 90\%$) to obtain a control set of command voltages. The initial coupling experiment was run at a safe repetition rate of 3 Hz with low noise. Since our evolutionary algorithm works by adding random noise to an initial state, we evaluated the settling time of the mirror by removing the selection step of the algorithm (see Fig. 4.6), leaving the control set intact from iteration to iteration while applying "noisy" control sets between measurements. For the best results, care was taken to assure that any other transient properties of the system were suppressed. For example, the detector response times were shorter than the tested set times, and the system was allowed time for any transient environmental or vibrational effects to subside.

We normalized the standard deviation of the measured coupling efficiency according to the best efficiency measured during testing, though this made little difference for high-efficiency coupling. After running the experiment, we obtained the results shown in Fig. A.7.

A.4.3 Correction

Based on the outcome of the settling-time measurements, it was straightforward to pick an appropriate set-time for the DM according to our required measurement accuracy. From our testing, we chose a set time of 250 ms since our evolutionary
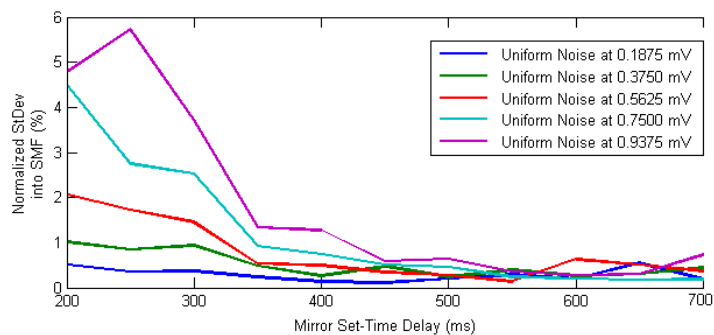
Figure A.7: Standard deviation of coupling efficiency with varying noise levels between measurements.

noise levels were generally between 0.125 and 0.35 mV, and we allowed for a small amount of random walk as discussed in Section 4.3.2. Note that it is possible to intentionally introduce randomness into the decision-making algorithm by operating the mirror faster than the required settling time. This method may allow for a significant speed increase for algorithms which rely on noise in some way, e.g., SA/GESA algorithms.

REFERENCES

[1] D. DiVincenzo, "The physical implementation of quantum computation," *Fortschr. Phys.*, vol. 48, pp. 771–783, 2000.

[2] E. Knill, R. Laflamme, and G. Milburn, "A scheme for efficient quantum computation with linear optics," *Nature*, vol. 409, pp. 46–52, 2001.

[3] R. G. Wilson, "Ball-lens coupling efficiency for laser-diode to single-mode fiber: Comparison of independent studies by distinct methods," *Appl. Opt.*, vol. 37, no. 15, pp. 3201–3205, 1998.

[4] L. O. Lierstuen and A. S. Sudbø, "Coupling losses between standard single-mode fibers and rectangular waveguides for integrated optics," *Appl. Opt.*, vol. 34, no. 6, pp. 1024–1028, 1995.

[5] F. Gonté, A. Courteville, and R. Dändliker, "Optimization of a single-mode fiber coupling efficiency with an adaptive membrane mirror," *Opt. Eng.*, vol. 41, no. 5, pp. 1073–1076, 2002.

[6] M. L. Plett, P. R. Barbier, and D. W. Rush, "Compact adaptive optical system based on blind optimization and a micromachined membrane deformable mirror," *Appl. Opt.*, vol. 40, no. 3, pp. 327–330, 2001.

[7] M. Born and E. Wolf, *Principles of Optics*, 7th ed. Cambridge, UK: Cambridge University Press, 1999.

[8] E. Hecht, *Optics*, 4th ed. San Francisco, CA: Addison-Wesley, 1995.

[9] B. E. A. Saleh and M. Teich, *Fundamentals of Photonics*, 1st ed. New York, NY: Wiley-Interscience, 1991.

[10] M. Schwertner, M. J. Booth, and T. Wilson, "Wavefront sensing based on rotated lateral shearing interferometry," *Opt. Comm.*, vol. 281, pp. 210–216, 2008.

[11] G. W. R. Leibbrandt, G. Harbers, and P. J. Kunst, "Wave-front analysis with high accuracy by use of a double-grating lateral shearing interferometer," *Appl. Opt.*, vol. 35, no. 31, pp. 6151–6161, 1996.

[12] F. Jenkins and H. White, *Fundamentals of Optics*. New York, NY: McGraw-Hill, 1957.

[13] E. J. Fernández, L. Vabre, B. Hermann, A. Unterhuber, B. Považay, and W. Drexler, "Adaptive optics with a magnetic deformable mirror: Applications in the human eye," *Opt. Exp.*, vol. 14, no. 20, pp. 8904–8917, 2006.

[14] E. Li, Y. Dai, H. Wang, and Y. Zhang, "Application of eigenmode in the adaptive optics system based on a micromachined membrane deformable mirror," *Appl. Opt.*, vol. 45, no. 22, pp. 5651–5656, 2006.

[15] D. R. Neal, J. Copland, and D. Neal, "Shack-Hartmann wavefront sensor precision and accuracy," in *Proc. of SPIE*, ser. Advanced Characterization Techniques for Optical, Semiconductor, and Data Storage Components, vol. 4779, 2002, pp. 148–160.

[16] Y. Dai, F. Li, X. Cheng, Z. Jiang, and S. Gong, "Analysis on Shack-Hartmann wave-front sensor with fourier optics," *Opt. & Lsr. Tech.*, vol. 39, pp. 1374–1379, 2007.

[17] H. Choo and R. Muller, "Addressable microlens array to improve dynamic range of Shack-Hartmann sensors," *J. Micro. Sys.*, vol. 15, no. 6, pp. 1555–1567, 2006.

[18] L. Mandel and E. Wolf, *Optical Coherence and Quantum Optics*. Cambridge, UK: Cambridge University Press, 1995.

[19] S. Chuang, *Physics of Optoelectronic Devices*. New York, NY: Wiley, 1995.

[20] D. Gloge, "Weakly guiding fibers," *Appl. Opt.*, vol. 10, no. 10, pp. 2252–2258, 1971.

[21] V. N. Mahajan, "Strehl ratio of a Gaussian beam," *J. Opt. Soc. Am. A*, vol. 22, no. 9, pp. 1824–1833, 2005.

[22] J. J. Field, T. A. Planchon, W. Amir, C. G. Durfee, and J. A. Squier, "Characterization of a high efficiency, ultrashort pulse shaper incorporating a reflective 4096-element spatial light modulator," *Opt. Comm.*, vol. 278, pp. 368–376, 2007.

[23] V. Durán, V. Climent, E. Tajahuerce, Z. Jaroszewicz, J. Arines, and S. Bará, "Efficient compensation of Zernike modes and eye aberration patterns using low-cost spatial light modulators," *J. Biomed. Opt.*, vol. 12, no. 1, pp. 014 037–1–014 037–6, 2007.

[24] S. Serati and J. Stockley, "Advances in liquid crystal based devices for wavefront control and beamsteering," in *Proc. of SPIE*, vol. 5894, 2005, pp. 180–192.

[25] J. W. Judy, "Microelectromechanical systems (MEMS): Fabrication, design and applications," *Smart Mater. Struct.*, vol. 10, pp. 1115–1134, 2001.

[26] D. J. Dagel, W. D. Cowan, O. B. Spahn, G. D. Grossetete, A. J. Griñe, M. J. Shaw, P. J. Resnick, and B. Jokiel, "Large-stroke MEMS deformable mirrors for adaptive optics," *J. of MEMS*, vol. 15, no. 3, pp. 572–583, 2006.

[27] N. Devaney, D. Coburn, C. Coleman, J. C. Dainty, E. Dalimier, T. Farrell, D. Lara, D. Mackey, and R. Mackey, "Characterisation of MEMs mirrors for use in atmospheric and ocular wavefront correction," in *Proc. of SPIE*, vol. 6888, 2008, pp. 688 801–688 810.

[28] E. Dalimier and C. Dainty, "Comparitive analysis of deformable mirrors for ocular adaptive optics," *Opt. Exp.*, vol. 13, no. 11, pp. 4275–4285, 2005.

[29] Imagine Optic SA, "Adaptive optics components and software," December 2008. [Online]. Available: http://imagine-optic.com/.

[30] G. Golub and W. Kahan, "Calculating the singular values and pseudo-inverse of a matrix," *J. of the Soc. for Ind. and Appl. Mathematics, Series B: Numerical Anal.*, vol. 2, no. 2, pp. 205–224, 1965.

[31] S. E. Winters, J. H. Chung, and S. A. Velinsky, "Modeling and control of a deformable mirror," *J. Dyn. Sys. Meas. & Cont.*, vol. 124, pp. 297–302, 2002.

[32] P. C. Hansen, "Truncated singular value decomposition solutions to discrete ill-posed problems with ill-determined numerical rank," *SIAM J. on Sci. and Stat. Comp.*, vol. 11, no. 3, pp. 503–518, 1990.

[33] P. Carney, "An algebraic approach to the Radon transform," class notes for ECE 569, Department of Electrical and Computer Engineering, University of Illinois at Urbana-Champaign, Fall 2007.

[34] S. Bonora, I. Capraro, L. Poletto, M. Romanin, C. Trestino, and P. Villoresi, "Wave front active control by a digital-signal-processor-driven deformable membrane mirror," *Rev. Sci. Instrum.*, vol. 77, no. 9, pp. 093 102–1–093 102–5, 2006.

[35] M. L. Plett, P. R. Barbier, and D. W. Rush, "Blind optimization of optical power into a single mode optical fiber using a MEMS deformable membrane mirror," *Appl. Opt.*, vol. 40, no. 3, pp. 327–330, 2001.

[36] S. Boyd and L. Vandenberghe, *Convex Optimization*. Cambridge, UK: Cambridge University Press, 2004.

[37] T. Weyrauch, M. A. Vorontsov, J. W. Gowens, and T. G. Bifano II, "Fiber coupling with adaptive optics for free-space optical communication," in *Proc. of SPIE*, vol. 4489, 2002, pp. 177–184.

[38] L. Zhu, P.-C. Sun, D.-U. Bartsch, W. R. Freeman, and Y. Fainman, "Wave-front generation of Zernike polynomial modes with a micromachined membrane deformabel mirror," *Appl. Opt.*, vol. 38, no. 28, pp. 6019–6026, 1999.

[39] P. P. C. Yip and Y.-H. Pao, "A guided evolutionary simulated annealing approach to the quadratic assignment problem," *IEEE Trans. Syst. Man Cybernet*, vol. 24, pp. 1383–1387, 1994.

[40] S. Kirkpatrick, C. D. Gelatt Jr., and M. P. Vecchi, "Optimization by simulated annealing," *Science*, vol. 220, no. 4598, pp. 671–680, 1983.

VITA

Scott M. Jobling

Contact Information

Department of Physics

The University of Illinois at Urbana-Champaign   *Cell Phone:* (774) 521-9945

251 Loomis Laboratory   *Office Phone:* (217) 244-1608

1110 W. Green St.   *Fax:* (217) 244-7559

Urbana, IL 61801 USA   *E-mail:* jobling2@illinois.edu

Education

The University of Illinois at Urbana-Champaign, Urbana, Illinois USA

M.S., Electrical and Computer Engineering, Expected: Oct. 2008 (3.87/4.0 GPA)

- Thesis Topic: Adaptive Optics for Improved Mode-Coupling Efficiencies
- Advisor: Professor Paul G. Kwiat
- Area of Study: Adaptive Optics

The University of Massachusetts at Lowell, Lowell, MA USA

B.S., Electrical and Computer Engineering, June 2006 (3.93/4.0 GPA)

- *Summa cum Laude*, Salutatorian in Electrical Engineering
- Emphasis: photonics and fiber optics

Awards

The University of Illinois at Urbana-Champaign

- Outstanding Teaching Assistant Award, 2006-2007
- Best Student Poster - OSA UIUC Chapter, OSA Workshop, 2008

The University of Massachusetts at Lowell

- RESNA Student Design Competition National Finalist, 2006
- Daniel C. Cole Undergraduate Research Award, 2006
- Carl Stevens Academic Achievement Award, 2006
- Raytheon Electrical Engineering Scholarship, 2006
- James Alexander Dirko Scholarship, 2006
- ISET Scholar, 2005
- Charles J. Hoff Scholarship, 2005-2006
- Dean's and Chancellor's Scholarships, 2002-2006

Academic Experience

The University of Illinois at Urbana-Champaign, Urbana, IL USA

Graduate Research Assistant   **January 2007 to present**

- Kwiat Quantum Information Group (Jan. 2007 to present)

Researched the practical limits of efficient mode-coupling correction using 52-actuator adaptive-optic mirror. Required optical design and implementation, MATLAB and C/C++ interfacing, and development of capable control algorithm. Further testing performed with manufacturer's software for direct mirror control and wavefront analysis (Mirao52D, HASO3, CASAO).

- Sandia National Labs Optical Mems Group (May 2007 to July 2007)

  Evaluated the potential of a hexagonal 61-element MEMS mirror for use in fiber-to-fiber coupling optimization. Required MATLAB interfacing, optical implementation, and interferometric testing through a Veeco system.

Graduate Teaching Assistant   **August 2006 to May 2007**

- Introduction to Electrical and Computer Engineering (Fall and Spring)

  Responsible for instruction of freshman/sophomore level laboratory. Experimental introduction of many topics from I/V Curves through single-transistor circuits and logic design.

The University of Massachusetts at Lowell, Lowell, MA USA

Undergraduate Researcher   **December 2004 to June 2006**

ECE Senior Design - Assistive Technology Program (Nov. 2005 to June 2006)

- Carried out the desires of staff at a local home for multiply disabled adults to create a highly sensory educational device for cognitive and fine-motor skill development. Involved idea-to-delivery design and construction of 400 LED-based display with capable wireless control. Worked with BasicStamp microcontrollers, RF wireless, touchpad electronics, PCB design, and hardware construction.

Penn State University EE REU (May 2005 to Aug. 2005)

- Studied switching properties of the liquid crystal MLC-2048, specifically to exploit dual-frequency behavior for faster switching times. Performed optical design and setup, and worked with MATLAB, Mathematica, and Origin.

ISET Research Scholar (Dec. 2004 to April 2005)

- Investigated adaptive filtering techniques used in telecommunication systems for countering ISI degradation. Performed simulations in FORTRAN.

Publications

S. Jobling, K. T. McCusker, P. G. Kwiat, "Adaptive optics for improved mode-coupling efficiencies," in *FiO 2008/LS XXIV/PM/OFT on CD* (2008), JWA32.

S. Jobling, "Development of a touch-controlled display for cause/effect and snoezelen type therapy," in *RESNA 2007 Conf. on CD* (2007).

S. Jobling, Y. Williams, J. Liou, and I. C. Khoo, "Low voltage behavior and electro-optical switching times of dual-frequency nematic liquid crystals," in *NSF EEREU Penn State*, vol. 3, August 2005. [Online]. Available: http://www.ee.psu.edu/reu/All_journal/2005V3/REUV3_p92p102.pdf.

Professional Experience

Microwave Device Technology, Westford, MA USA

Co-Op Intern in Wafer-Testing Station   **January 2006 to March 2006**

- Aided in bringing flip-chip functionality to automated probing station, up-dating procedures for new GUI and hardware, and testing sample wafers for verification.

Technical Skills

Optics: Two years experience with bulk-optical design and alignment, fiber-coupling techniques, and adaptive-optic optimization. Knowledge of Gaussian optics, diffraction, coherence theory.

Control theory: Knowledge of relevant control algorithms for adaptive optics, including genetic, evolutionary, simulated annealing / GESA, and convex opti-mization techniques.

Programming: MATLAB, C, C++, pBASIC, FORTRAN

Data Analysis: MATLAB, Mathematica, Microsoft Excel, Origin

Technical/Specific Software: Veeco, CASAO, HASO Suite, Mirao, Zemax, DataRay, Thorlabs APTUser

Applications: Microsoft Office, Microsoft Visual Studio, OpenOffice, Adobe Suite, LaTeX